Multi-Scale Single-Bit *RP-EMS* Synthesis for Advanced Propagation Manipulation Through System-by-Design

Giacomo Oliveri, *Senior Member, IEEE*, Paolo Rocca, *Senior Member, IEEE*, Marco Salucci, *Senior Member, IEEE*, Danilo Erricolo, *Fellow, IEEE*, and Andrea Massa, *Fellow, IEEE*

***Abstract*— A new method for the synthesis of *single-bit reconfigurable passive electromagnetic skins* (1RP-EMSs) featuring advanced beam shaping capabilities is proposed. By using single-bit unit cells, the multiscale problem of controlling 1RP-EMSs is formulated as a two-phase process. First, the macroscale synthesis of the discrete surface current that radiates the electromagnetic (EM) field fitting the user-designed requirements is performed by means of an innovative quantized version of the iterative projection method (QIPM). Subsequently, the meta-atom states of the 1RP-EMS are optimized with a customized implementation of the *System-by-Design* paradigm to yield a 1RP-EMS that supports such a feasible reference current. A representative set of numerical results is reported to assess the effectiveness of the proposed approach in designing and controlling single-bit meta-atom RP-EMSs that enable complex wave manipulations.**

***Index Terms*— Electromagnetic (EM) holography, iterative projection method, metamaterials, next-generation communications, reconfigurable EM skins, reconfigurable intelligent surfaces, System-by-Design (SbD).**

Manuscript received 19 February 2022; revised 18 June 2022; accepted 5 August 2022. Date of publication 2 September 2022; date of current version 9 November 2022. This work was supported in part by the Project Cloaking Metasurfaces for a New Generation of Intelligent Antenna Systems (MANTLES) under Grant 2017BHFZKH funded by the Italian Ministry of Education, University, and Research through the PRIN2017 Program (CUP: E64I19000560001), in part by the Project SPEED under Grant 61721001 funded by the National Science Foundation of China through the Chang-Jiang Visiting Professorship Program, in part by the project Inversion Design Method of Structural Factors of Conformal Load-Bearing Antenna Structure Based on Desired EM Performance Interval under Grant 2017HZJXSZ funded by the National Natural Science Foundation of China, and in part by the project Research on Uncertainty Factors and Propagation Mechanism of Conformal Load-Bearing Antenna Structure under Grant 2021JZD-003 funded by the Department of Science and Technology of Shaanxi Province within the Program Natural Science Basic Research Plan in Shaanxi Province. *(Corresponding author: Andrea Massa.)*

Giacomo Oliveri and Marco Salucci are with the ELEDIA Research Center (ELEDIA@UniTN), Department of Civil, Environmental, and Mechanical Engineering (DICAM), University of Trento, 38123 Trento, Italy (e-mail: giacomo.oliveri@unitn.it; marco.salucci@unitn.it).

Paolo Rocca is with the ELEDIA Research Center (ELEDIA@UniTN), Department of Civil, Environmental, and Mechanical Engineering (DICAM), University of Trento, 38123 Trento, Italy, and also with the ELEDIA Research Center (ELEDIA@XIDIAN), Xidian University, Xi'an, Shaanxi 710071, China (e-mail: paolo.rocca@unitn.it).

Danilo Erricolo is with the Andrew Electromagnetics Laboratory, Department of Electrical and Computer Engineering, University of Illinois at Chicago, Chicago, IL 60607 USA (e-mail: derric1@uic.edu).

Andrea Massa is with the ELEDIA Research Center (ELEDIA@UESTC-UESTC), School of Electronic Science and Engineering, University of Electronic Science and Technology of China (UESTC), Chengdu 611731, China, also with the ELEDIA Research Center (ELEDIA@UniTN - University of Trento), Department of Civil, Environmental, and Mechanical Engineering (DICAM), 38123 Trento, Italy, and also with the ELEDIA Research Center (ELEDIA@TSINGHUA - Tsinghua University), Beijing 100084, China (e-mail: andrea.massa@unitn.it).

Color versions of one or more figures in this article are available at https://doi.org/10.1109/TAP.2022.3201700.

Digital Object Identifier 10.1109/TAP.2022.3201700

I. Introduction and Rationale

ELECTROMAGNETIC skins (EMSs) are currently the core of a theoretical, methodological, and practical revolution within the academic and industrial communities working on wireless communications [1], [2], [3], [4], [5], [6], [7], [8], [9], [10]. Several research studies on the foundation, the modeling, the simulation, the design, and the test of EMSs are currently under development with a strong interdisciplinary effort combining chemistry, physics, metamaterial science, electromagnetic (EM) engineering, telecommunications, and signal processing expertises [1], [2], [3], [7], [8]. As a matter of fact, starting from their early conceptualization as thin metasurfaces are able to manipulate the wave propagation beyond Snell's laws [11], EMSs are considered as one of the key enabling factors of the revolutionary *smart EM environment* (SEME) paradigm in wireless communications [4], [5], [6], [12], [13]. This is motivated by the possibility that they enable to control the EM reflected power in user-defined directions/regions, hence potentially improving the coverage/quality of the resulting wireless network (see Fig. 1). Nevertheless, a multiplicity of methodological and practical challenges [2], [3], [4], [8], [10], [11], [14] still needs to be addressed to have a full transition from traditional wireless systems to the SEME-enhanced ones.

In particular, the *complexity* associated with the design, fabrication, implementation, control, and integration within a wireless scenario of EMSs is the main critical issue. More specifically, complexity arises:

1) at the EMS design level, owing to the multiscale nature of its layout that features microscale/nanoscale descriptors combined with meso/macroscale reflection and communication properties;
2) at the SEME level, due to the interactions between the EMSs and the large-scale propagation scenario;
3) at the "propagation management" level, because of the need to fruitfully integrate the EMSs in a heterogenous wireless infrastructure, which includes the base stations, the integrated access and backhaul (IAB) nodes, and the smart repeaters to yield measurable performance improvements in the overall wireless network.

Within such a framework, the design of planar artificial materials with advanced propagation management capabilities has been recently demonstrated for *static passive EMSs* (SP-EMSs) by exploiting artificial intelligence (AI) techniques

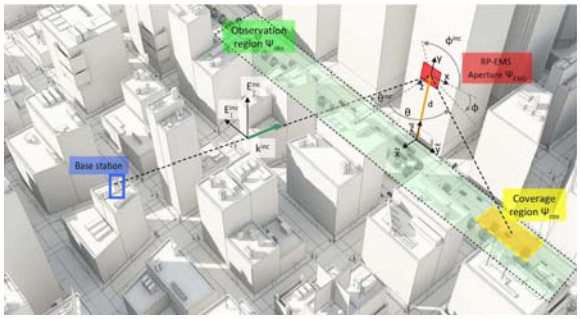

Fig. 1. *Problem geometry*. Sketch of the SEME scenario.

within the *System-by-Design* (SbD) paradigm [5], [6], [15]. Such an approach leverages on the decomposition of the problem at hand into a source design phase and a subsequent optimization of the surface descriptors of the SP-EMS within the *generalized sheet transition condition* (GSTC) framework [5], [6], [11]. Thanks to the modularity of such a synthesis tool and its multiscale-oriented nature, the efficient design of wide-aperture EMSs that enable advanced pattern shaping properties has been carried out despite the use of extremely simple unit cells.

Otherwise, *reconfigurable passive EMSs* (RP-EMSs) have been proposed and widely studied to dynamically control the propagation environment for adaptively improving the communication performance [1], [2], [3], [7], [16]. Toward this end, RP-EMS unit cells need either analog (e.g., varactors/varistor [9], [14], [17] and mechanically tuned subparts [10]) or digitally controlled (e.g., p-i-n diodes [18]) components. From an applicative viewpoint, the implementation of a continuous control on each RP-EMS cell can yield to very expensive and complex architectures; thus, it is generally avoided [19]. The RP-EMS analog states are, thus, often discretized using few bits, B, per cell [9], [19], or they are implemented by using binary switches [18]. Therefore, RP-EMSs are usually digitally controlled systems [18], [19], [20] with relatively limited per-cell degrees of freedom (DoFs) compared to SP-EMSs [5], [6].

A key consequence of such a per-cell constraint, mainly when low-bit ($B \rightarrow 1$) RP-EMS are at hand [19], turns out to be the very limited control of the shape of the reflected beam [19]. Thus, the mainstream state-of-the-art literature on RP-EMSs has been concerned with the synthesis of RP-EMSs with "simple" anomalous reflection capabilities and narrow beam focusing (i.e., pencil beam-like) [9], [18], [19], [20]. However, demonstrating more advanced footprint control/shaping with a digital RP-EMS would be of great interest in practice since it would allow one to efficiently concentrate the reflected power in arbitrary desired areas (i.e., roads, squares, streets, and buildings) and not just in spots. Unfortunately, the approach derived in [5] and [6] to design SP-EMSs affording shaped footprint patterns cannot be directly applied to RP-EMSs. Indeed, the synthesis of the reference surface current, which is performed in the first step of [5] and [6] exploiting the nonuniqueness of the associated inverse source (IS) problem to take advantage of the *nonradiating currents* (NRCs) [5], [21], assumes that the unit cell of the corresponding EMS allows fine-tuning of the reflection phase. By definition, this is actually prevented when dealing with digital RP-EMSs [19], hence making the design process ineffective and potentially unable to fulfill complex coverage requirements.

Dealing with RP-EMSs, the objective of this work is twofold. On the one hand, it is aimed at presenting and validating an innovative method for the synthesis (i.e., the design and the control) of high-performance holographic single-bit RP-EMSs (1RP-EMSs). More specifically, the proposed method is conceived to address two fundamental challenges in RP-EMS engineering, that is: 1) the identification of the geometry/features of the 1RP-EMS structure (i.e., the physical layout of the unit cells enabling the desired reconfiguration capabilities) and 2) its optimal time-varying control setup to enable the desired wireless coverage (see Fig. 1). On the other hand, it is devoted to proving that minimum complexity RP-EMSs can be used in SEME scenarios to yield complex wave propagation phenomena (i.e., contoured footprint patterns with arbitrary shapes) despite the coarse tuning of the reflection phase.

Starting from the design of a meta-atom of the RP-EMS that features only a single-bit reconfiguration and by generalizing the theoretical concepts on complex large-scale EM wave manipulation systems [5], [6], [22], [23], [24], [25], the first step of the proposed method for the synthesis of 1RP-EMSs deals with the computation of a discrete-phase current that radiates a field distribution fitting complex footprint patterns. A digital SbD-based RP-EMS optimization is then carried out to set the 1RP-EMS configuration that supports such a reference discrete-phase current. Toward this end, suitable AI paradigms are exploited for building reliable and computationally efficient "RP-EMS digital-twins" (DTs) that properly address the issues related to the multiscale complexity of the problem at hand.

The outline of this article is given as follows. First, the 1RP-EMS synthesis problem is formulated (see Section II). Section III then details the proposed two-step (i.e., design and control) synthesis method. Representative results from a wide set of numerical experiments are reported for assessment purposes, and comparisons with state-of-the-art techniques are considered as well (see Section IV). Finally, some concluding remarks follow (see Section V).

II. Mathematical Formulation

Let a 1RP-EMS be centered in the origin of the local coordinate system (x, y, z) (see Fig. 1). The 1RP-EMS consists of $M \times N$ reconfigurable binary meta-atoms displaced on a regular grid of cells with sides Δx and Δy on a planar region Ψ_{EMS} ($\Psi_{EMS} = \{-M \times (\Delta x/2) \leq x \leq M \times (\Delta x/2); -N \times (\Delta y/2) \leq y \leq N \times (\Delta y/2)\}$). Each (m, n)th ($m = 1, \ldots, M$; $n = 1, \ldots, N$) meta-atom is defined by a set of U geometrical/material descriptors $\mathbf{g} \triangleq \{g^{(u)}; u = 1, \ldots, U\}$, and it features, at the tth ($t = 1, \ldots, T$) time step, a binary state $s_{mn}(t) \in \{0, 1\}$.

The 1RP-EMS at the tth ($t = 1, \ldots, T$) instant can be univocally identified by the binary *microscale* state vector $\mathcal{S}(t)$, $\mathcal{S}(t) \triangleq \{s_{mn}(t); m = 1, \ldots, M; n = 1, \ldots, N\}$, and the time-independent *microscale* descriptor vector $\mathbf{g}$ (i.e., it is unrealistic to geometrically change the atom layout at each time step). The RP-EMS can be described from an EM viewpoint by the *microscale* electric/magnetic surface

susceptibility vector $\mathcal{K}(t)$ $(t = 1, \ldots, T)$ [5], [11], whose the (m, n)th entry $(m = 1, \ldots, M;\ n = 1, \ldots, N)$ is the diagonal tensor of the electric/magnetic local surface susceptibility of the (m, n)th meta-atom

$$\overline{\overline{K}}_{mn}(t) = \mathbb{K}\{\mathbf{g};\ s_{mn}(t)\} \tag{1}$$

being $\overline{\overline{K}}_{mn}(t) \triangleq \sum_{q=x,y,z} k_{qq}(\mathbf{g};\ s_{mn}(t))\widehat{q}\widehat{q}$.

According to the GSTC technique [11], [26], [27], the instantaneous far-field pattern, $\overline{E}(r, \theta, \varphi; t)$, reflected by the RP-EMS when illuminated by a time-harmonic plane wave at frequency f impinging from the incidence direction $(\theta^{inc}, \varphi^{inc})$ and characterized by "perpendicular" and "parallel" complex-valued electric field components $E_{\perp}^{inc}$ and $E_{\parallel}^{inc}$ is a function of the surface susceptibility vector $\mathcal{K}$ through the *macroscale* induced surface current $\overline{J}$ (i.e., $\overline{E}(r, \theta, \varphi; t) = \mathbb{F}\{\overline{J}(x, y; t)\}$). More in detail, it turns out to that [5], [6], [11], [32]

$$\begin{aligned}\overline{E}(r, \theta, \varphi; t) &= \frac{jk_0}{4\pi}\frac{\exp(-jk_0 r)}{r}\int_{-\frac{M\Delta x}{2}}^{\frac{M\Delta x}{2}}\int_{-\frac{N\Delta y}{2}}^{\frac{N\Delta y}{2}}\overline{J}(x', y'; t)\\ &\quad\times\exp\left[jk_0\left(rx'\sin\theta\cos\varphi + ry'\sin\theta\sin\varphi\right)\right]\mathrm{d}x'\mathrm{d}y'\end{aligned} \tag{2}$$

where the surface current $\overline{J}$ is given by

$$\overline{J}(x, y; t) = \widehat{\mathbf{r}}\times\left[\eta_0\widehat{\mathbf{r}}\times\overline{J}^{e}(x, y; t) + \overline{J}^{h}(x, y; t)\right] \quad (x, y) \in \Psi_{EMS} \tag{3}$$

where $\overline{J}^{o}$, $o \in \{e, h\}$, is the electric/magnetic component of the current induced on the RP-EMS, while $k_0 = 2\pi f(\varepsilon_0\mu_0)^{1/2}$ and $\eta_0 = (\mu_0/\varepsilon_0)^{1/2}$ are the free-space wavenumber and the impedance, respectively, which depends on the free-space permeability (permittivity) μ_0 (ε_0).

Subject to the local periodicity condition, the dependence of $\overline{J}^{o}$, $o \in \{e, h\}$, on the entries of the *microscale* electric/magnetic surface susceptibility vector $\mathcal{K}$ (i.e., $\overline{J}^{o}(x, y; t) = \mathbb{G}\{\mathbb{K}^{o}\{\mathbf{g};\ s_{mn}(t)\};\ \overline{E}^{inc}(x, y, 0; t)\}$, $o \in \{e, h\}$) is in the following form (i.e., explicit version of the operator $\mathbb{G}\{\cdot\}$) [5], [6], [11], [27]:

$$\begin{aligned}\overline{J}^{e}(x, y; t) &= \sum_{m=1}^{M}\sum_{n=1}^{N}\left\{j2\pi f\varepsilon_0\left[\overline{\overline{K}}_{mn}^{e}(t)\cdot\overline{E}_{mn}(t)\right]_{\tau}\right.\\ &\quad\left.-\widehat{\boldsymbol{\nu}}\times\nabla_{\tau}\left[\overline{\overline{K}}_{mn}^{h}(t)\cdot\overline{H}_{mn}(t)\right]_{\nu}\right\}\Omega_{mn}(x, y)\\ \overline{J}^{m}(x, y; t) &= \sum_{m=1}^{M}\sum_{n=1}^{N}\left\{j2\pi f\mu_0\left[\overline{\overline{K}}_{mn}^{h}(t)\cdot\overline{H}_{mn}(t)\right]_{\tau}\right.\\ &\quad\left.+\widehat{\boldsymbol{\nu}}\times\nabla_{\tau}\left[\overline{\overline{K}}_{mn}^{e}(t)\cdot\overline{E}_{mn}(t)\right]_{\nu}\right\}\Omega_{mn}(x, y)\end{aligned} \tag{4}$$

where $\widehat{\boldsymbol{\nu}}$ is the outward normal to Ψ_{EMS}, $[\,.\,]_{\tau/\nu}$ stands for the tangential/normal component, and $\Omega_{mn}(x, y) \triangleq \{1$ if $[-(m-M-1)\times(\Delta x/2) \le x \le (m-M)\times(\Delta x/2)]$ and $[-(n-N-1)\times-(\Delta y/2) \le y \le (n-N)\times(\Delta y/2)]$; 0 otherwise$\}$ is the basis function related to the (m, n)th $(m = 1, \ldots, M;\ n = 1, \ldots, N)$ cell with support $\Delta\Psi_{EMS}$ $(\Delta\Psi_{EMS} \triangleq \Delta x \times \Delta y)$, while $\overline{E}_{mn}$ $(\overline{H}_{mn})$ is the surface averaged electric (magnetic) field (see the Appendix).

Such a derivation points out that the tth $(t = 1, \ldots, T)$ far-field pattern $\overline{E}(r, \theta, \varphi; t)$ can be controlled by properly adjusting the $M \times N$ binary entries of $\mathcal{S}(t)$ once the 1RP-EMS has been designed (i.e., $\mathbf{g}$ is set; see Section II-A). Accordingly, the problem at hand can be mathematically formulated as follows.

1RP-EMS Synthesis Problem: Find the optimal setting of the microscale descriptor vector, $\mathbf{g}^{opt}$, and the optimal configuration of T binary *microscale* state vectors, $\{\mathcal{S}^{opt}(t);\ t = 1, \ldots, T\}$ such that

$$\Phi(\mathbf{g}, \mathcal{S}(t)) = \int_{\Psi_{obs}}\Re\left\{F^{des}(\widetilde{x}, \widetilde{y}, \widetilde{z}; t) - F(\widetilde{x}, \widetilde{y}, \widetilde{z}; t)\right\}\mathrm{d}\widetilde{x}\mathrm{d}\widetilde{y}\mathrm{d}\widetilde{z} \tag{5}$$

is minimized at each tth $(t = 1, \ldots, T)$ time instant [i.e., $(\mathbf{g}^{opt}, \mathcal{S}^{opt}(t)) = \arg\,(\min_{\mathbf{g},\mathcal{S}(t)}[\Phi(\mathbf{g}, \mathcal{S}(t))])$, $t = 1, \ldots, T$].

In (5), $\Re\{\,.\,\}$ is the "ramp" function, and $F^{des}(\widetilde{x}, \widetilde{y}, \widetilde{z}; t)$ is the user-defined power pattern footprint at the tth $(t = 1, \ldots, T)$ time instant in the observation region Ψ_{obs}, with $(\widetilde{x}, \widetilde{y}, \widetilde{z})$ being the RP-EMS global coordinate system (see Fig. 1). Moreover, the footprint pattern is a function of the reflected far-field pattern $\overline{E}(r, \theta, \varphi; t)$ (i.e., $F(\widetilde{x}, \widetilde{y}, \widetilde{z}; t) = \mathbb{H}\{\overline{E}(r, \theta, \varphi; t)\}$), and it is given by

$$F(\widetilde{x}, \widetilde{y}, \widetilde{z}; t) = \left|\overline{E}\left(\sqrt{\widetilde{x}^2 + \widetilde{y}^2 + (\widetilde{z} - d)^2}\right.\right.\\ \left.\left.\arctan\frac{\sqrt{\widetilde{y}^2 + (\widetilde{z} - d)^2}}{\widetilde{x}}, \arctan\left(\frac{\widetilde{z} - d}{\widetilde{x}}\right); t\right)\right|^2 \tag{6}$$

where d is the 1RP-EMS height over the ground plane (see Fig. 1).

It is worth noticing that, unlike the case of SP-EMSs, the synthesis of a 1RP-EMS cannot be done by minimizing (5) only once. In fact, there is a different optimal configuration $\mathcal{S}^{opt}(t)$ for each tth $(t = 1, \ldots, T)$ user-defined footprint pattern, $F^{des}(\widetilde{x}, \widetilde{y}, \widetilde{z}; t)$, as pointed out in the following expression:

$$\begin{aligned}\Phi(\mathbf{g}, \mathcal{S}(t)) &= \int_{\Psi_{obs}}\Re\left\{F^{des}(\widetilde{x}, \widetilde{y}, \widetilde{z}; t)\right.\\ &\quad\left.-\mathbb{H}\left\{\mathbb{F}\left\{\mathbb{G}\left\{\mathbb{K}\{\mathbf{g};\ s_{mn}(t)\};\ \overline{E}^{inc}(x, y, 0; t)\right\}\right\}\right\}\right\}\\ &\quad\times\mathrm{d}\widetilde{x}\mathrm{d}\widetilde{y}\mathrm{d}\widetilde{z}\end{aligned} \tag{7}$$

where the link between $F^{des}(\widetilde{x}, \widetilde{y}, \widetilde{z}; t)$ and $\mathcal{S}(t) \triangleq \{s_{mn}(t);\ m = 1, \ldots, M;\ n = 1, \ldots, N\}$ is made evident. On the other hand, the U geometrical/material entries of $\mathbf{g}^{opt}$ must be set once as the optimal tradeoff among all T propagation scenarios.

Furthermore, the problem at hand is more complex than that of a multibit RP-EMS and (even) much more than of an SP-EMS. Unlike the SP case, the tth $(t = 1, \ldots, T)$ *microscale* electric/magnetic surface susceptibility vector $\mathcal{K}(t)$ assumes here only a quantized set of states (i.e., $2^{M\times N}$) instead of a continuity of values [5], [6]. Thus, the macroscale (reflection) properties of the arising EMS turn out to be more severely constrained than those of an SP-EMS or a multibit RP-EMS. Consequently, the fulfillment of complex shaping requirements on the footprint power pattern, as those in [5]

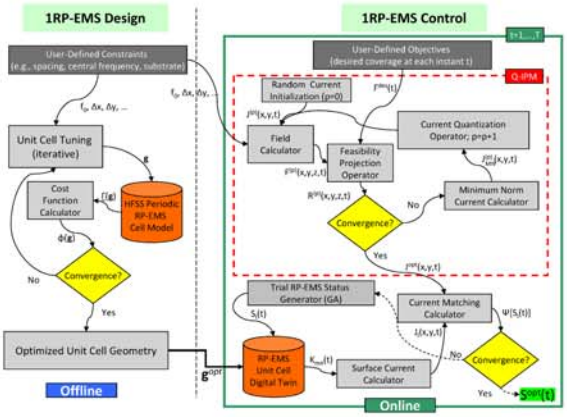

Fig. 2. Flowchart of the proposed design/control solution methods.

and [6], is certainly more difficult, and it may result in even physically unfeasible.

Taking into account these considerations, the "*1RP-EMS synthesis problem*" (5) is then addressed with a two-step approach (see Fig. 2) where the "*1RP-EMS design problem*" (see Section II-A) is first solved by identifying the U geometrical/material descriptors of the single-bit meta-atom (i.e., $\mathbf{g} \leftarrow \mathbf{g}^{opt}$), while the second step is aimed at setting the entries of the *microscale* state vector $\mathcal{S}(t)$ at each tth ($t = 1, \ldots, T$) time-instant to fulfill the footprint pattern requirements [i.e., $\mathcal{S}(t) \leftarrow \mathcal{S}^{opt}(t)$] ("*1RP-EMS control problem*"; see Section II-B).

A. 1RP-EMS Design Problem

As for the 1RP-EMS unit cell design (i.e., "offline" step; see Fig. 2), a key challenge and preparatory step to enable the footprint pattern control (i.e., $F \rightarrow F^{des}$) is the choice of a meta-atom structure whose reflection properties can be suitably modified when its logical state is changed [11]. In principle, an optimal tradeoff should be found by minimizing (7) with respect to $\mathbf{g}$ across all T user requirements $\{F^{des}(\widetilde{x}, \widetilde{y}, \widetilde{z}; t);\ t = 1, \ldots, T\}$. A "worst case"-strategy is adopted in this article to yield a more general and flexible implementation.

The design is then carried out by requiring that the 1RP-EMS meta-atom supports the widest possible reflection variation to account for not only the T propagation scenarios at hand but also, more in general, the largest range of admissible conditions. According to (4), such a guideline corresponds to the maximization of the gap between the values of the electric/magnetic local surface susceptibility when switching the status of the generic (m, n)th ($m = 1, \ldots, M$; $n = 1, \ldots, N$) meta-atom from $s_{mn}(t) = 0$ to $s_{mn}(t) = 1$. Mathematically, this means minimizing the following cost function:

$$\phi(\mathbf{g}) = \frac{1}{\pi^2}\left[\left(\left|\angle\Gamma_{mn}^{\perp\perp}(t)\right|_{f=f_0}^{s_{mn}(t)=1} - \angle\Gamma_{mn}^{\perp\perp}(t)\Big|_{f=f_0}^{s_{mn}(t)=0}\right| - \pi\right)^2 + \left(\left|\Gamma_{mn}^{\parallel\parallel}(t)\right|_{f=f_0}^{s_{mn}(t)=1} - \angle\Gamma_{mn}^{\parallel\parallel}(t)\Big|_{f=f_0}^{s_{mn}(t)=0}\right| - \pi\right)^2\right] \tag{8}$$

to yield the optimal set of the geometrical/material descriptors of the single-bit meta-atom, $\mathbf{g}^{opt}$ [i.e., $\mathbf{g}^{opt} = \arg(\min_{\mathbf{g}}[\phi(\mathbf{g})])$]. In (8), f_0 is the central working frequency, $\angle\cdot$ stands for the phase of the complex argument, and $\Gamma_{mn}^{\perp\perp}(t) = \mathbb{Y}^{\perp\perp}\{\mathbf{g};\ s_{mn}(t)\}$ and $\Gamma_{mn}^{\parallel\parallel}(t) = \mathbb{Y}^{\parallel\parallel}\{\mathbf{g};\ s_{mn}(t)\}$ are the TE/TM copolar components of the reflection tensor in the (m, n)th ($m = 1, \ldots, M$; $n = 1, \ldots, N$) cell, $\overline{\overline{\Gamma}}_{mn}(t)$, while the logical status of the (m, n)th cell (i.e., $s_{mn}(t) \in \{0, 1\}$) is physically implemented by biasing the diodes in the meta-atom layout (see Fig. 3), with $\mathbb{Y}$ being the implicit physical relation between the unit cell descriptors and its reflection properties.

B. 1RP-EMS Control Problem

Once the 1RP-EMS has been designed by setting $\mathbf{g}^{opt}$, the computation of $\mathcal{S}^{opt}(t)$ (i.e., "online" step; see Fig. 2) should be performed by minimizing the constrained ($\mathbf{g} \equiv \mathbf{g}^{opt}$) version of (5)

$$\Phi\left(\mathbf{g}^{opt}, \mathcal{S}(t)\right) = \int_{\Psi_{obs}} \Re\Big\{F^{des}(\widetilde{x}, \widetilde{y}, \widetilde{z}; t) - \mathbb{H}\Big\{\mathbb{F}\Big\{\mathbb{G}\Big\{\mathbb{K}\{\mathbf{g}^{opt};\ s_{mn}(t)\};\ \overline{E}^{inc}(x, y, 0; t)\Big\}\Big\}\Big\}\Big\} \times \mathrm{d}\widetilde{x}\mathrm{d}\widetilde{y}\mathrm{d}\widetilde{z} \tag{9}$$

[i.e., $\mathcal{S}^{opt}(t) = \arg(\min_{\mathcal{S}}[\Phi(\mathbf{g}^{opt}, \mathcal{S}(t))])$], which directly relates the state vector $\mathcal{S}(t)$ with the footprint target $F^{des}(\widetilde{x}, \widetilde{y}, \widetilde{z}; t)$. However, when dealing with *aperiodic* wave manipulation devices [5], [28], [29], [30], [31], such a single-phase solution approach is usually avoided in favor of splitting the problem at hand into two parts.

The former phase ("*reference current computation*") addresses a *macroscale* objective that consists of the computation of an ideal equivalent surface current $\overline{J}^{opt}(x, y; t)$ that affords the desired footprint pattern $F^{des}(\widetilde{x}, \widetilde{y}, \widetilde{z}; t)$, which is coded into the following macroscale cost function:

$$\Phi\left(\overline{J}(x, y; t)\right) = \int_{\Psi_{obs}} \Re\Big\{F^{des}(\widetilde{x}, \widetilde{y}, \widetilde{z}; t) - \mathbb{H}\Big\{\mathbb{F}\Big\{\overline{J}(x, y; t)\Big\}\Big\}\Big\}\mathrm{d}\widetilde{x}\mathrm{d}\widetilde{y}\mathrm{d}\widetilde{z} \tag{10}$$

to be minimized

$$\overline{J}^{opt}(x, y; t) = \arg\left(\min_{\overline{J}(x,y)}\left[\Phi\left(\overline{J}(x, y; t)\right)\right]\right). \tag{11}$$

The second (*microscale*) phase ("*1RP-EMS configuration*") [5], [28], [29], [30], [31] is devoted to choose the meta-atoms configuration $\mathcal{S}^{opt}(t)$ that supports the reference current $\overline{J}^{opt}(x, y; t)$ by solving the following optimization problem:

$$\mathcal{S}^{opt}(t) = \arg\left(\min_{\mathcal{S}}[\psi(\mathcal{S}(t))]\right) \tag{12}$$

where

$$\psi(\mathcal{S}(t)) \triangleq \frac{\left\|\overline{J}^{opt}(x, y; t) - \mathbb{G}\left\{\mathbb{K}\{\mathbf{g};\ s_{mn}(t)\};\ \overline{E}^{inc}(x, y, 0; t)\right\}\right\|}{\left\|\overline{J}^{opt}(x, y; t)\right\|}. \tag{13}$$

This two-phase process exploits the fast Fourier relation between currents and patterns (2), which results in very efficient implementations for large apertures [5], [28], [29], [30], [31]. Moreover, the arising currents can be reused

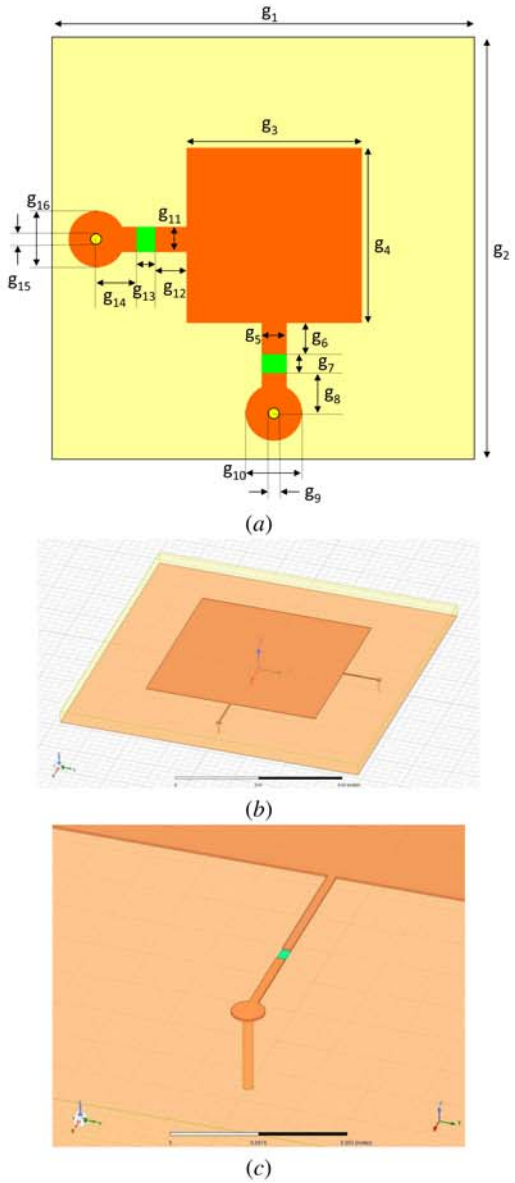

Fig. 3. *1RP-EMS design*—unit cell geometry: (a) top view and 3-D CAD model of (b) meta-atom and zoom on (c) switching device.

to design EMS arrangements with different unit cells [31]. Furthermore, the microscale synthesis step does not involve here the optimization of $\overline{\overline{K}}_{mn}$ to achieve ideal susceptibility distributions (which may yield, even in the SP-EMS case [5], [6], to nonfeasible anisotropy requirements on the cell), but it is aimed at setting the (m, n)th $(m = 1, \ldots, M; n = 1, \ldots, N)$ atom state $s_{mn}(t)$ that locally minimizes the mismatch with the target surface current.

On the other hand, it has to be noticed that the problem at hand requires, in principle, the phase of the wave reflected by the meta-atoms to vary over continuous intervals [5], [28], [29], [30], [31] regardless of the solution approach (direct or two-phases). This is clearly not true when dealing with B-bits RP-EMSs since each meta-atom can only assume 2^B states for each tth $(t = 1, \ldots, T)$ time instant. Such a limitation is even more critical for 1RP-EMSs $(B = 1)$. Moreover, despite the two-phase decomposition (see Fig. 2), the multiscale and quantized nature of the 1RP-EMS *control problem* still yields to a solution space with a size (i.e., $2^{M \times N}$) that grows exponentially with the RP-EMS aperture.

To take into account these pros and cons, a dedicated strategy needs to be implemented (see Section III).

III. Solution Method

While the "1RP-EMS *design*" problem (see Section II-A) is a quite standard real-variable optimization problem that can be addressed with a standard optimization tool, the *"1RP-EMS control"* one (see Section II-B) turns out to be a new challenge. The most intuitive strategy to solve this latter would be to exploit the methodology discussed in [5] by simply replacing the model of the local susceptibility dyadics of the SP-EMS with that of the reconfigurable single-bit meta-atom at hand. However, such an approach has a fundamental drawback when applied to the 1RP-EMS control. By ignoring the quantized nature of the 1RP-EMS surface currents in the "*reference current computation*" (11), there may not to be an implementable current distribution, $\overline{J}$ $(\overline{J}(x, y; t) = \mathbb{G}\{\mathbb{K}\{\mathbf{g}; s_{mn}(t)\}; \overline{E}^{inc}(x, y, 0; t)\})$, which approximates the synthesized reference current $\overline{J}^{opt}$, regardless of the approach to configure the 1RP-EMS (12). Therefore, an innovative method is proposed (see Section III-A) to compute a "feasible" ideal equivalent surface current $\overline{J}^{opt}$ that affords the desired footprint pattern F^{des}. The approach used in [5] for the design of an SP-EMS is then customized here to control the 1RP-EMS (see Section III-B).

A. QIPM-Based Reference Current Computation

In order to define a "feasible" reference current, a quantized version of the iterative projection method (QIPM) is derived.

Let $\mathcal{C}$ be the "*1RP-EMS current space*" composed of the whole set of the 1RP-EMS admissible surface currents having the following mathematical form:

$$\overline{J}(x, y; t) = \sum_{m=1}^{M} \sum_{n=1}^{N} \alpha_{mn}(t) \exp[j\chi_{mn}(t)] \Omega_{mn}(x, y) \widehat{\imath} \qquad (14)$$

where $\widehat{\imath}$ denotes the current polarization, while $\alpha_{mn}(t)$ $[\alpha_{mn}(t) = \mathbb{A}\{s_{mn}(t)\}]$ and $\chi_{mn}(t)$ $[\chi_{mn}(t) = \mathbb{X}\{s_{mn}(t)\}]$ are the values of the locally controlled magnitude and phase of the surface current that belongs to the discrete (two-element) alphabets $\mathcal{A}$ and $\mathcal{X}$, respectively. The elements of $\mathcal{A}$ and $\mathcal{X}$ are the magnitude and the phase of the current that each meta-atom can support when configured in one of its binary states, $s_{mn}(t) \in \{0, 1\}$, $(\mathcal{A} \triangleq \{\mathbb{A}\{s_{mn}(t) = 0\}, \mathbb{A}\{s_{mn}(t) = 1\}\}$, and $\mathcal{X} \triangleq \{\mathbb{X}\{s_{mn}(t) = 0\}, \mathbb{X}\{s_{mn}(t) = 1\}\})$.

Starting from a random initialization of the discrete coefficients $\alpha_{mn}^{(p)}(t)$ and $\chi_{mn}^{(p)}(t)$ $(m = 1, \ldots, M; n = 1, \ldots, N)$, whose values are randomly drawn from $\mathcal{A}$ and $\mathcal{X}$, the QIPM generates a succession of P trial current distributions, $\{\overline{J}^{(p)}; p = 1, \ldots, p\}$. First, the footprint pattern $F^{(p)}(\widetilde{x}, \widetilde{y}, \widetilde{z}; t)$ afforded by $\overline{J}^{(p)}$ is computed (2) and (6). It is then projected into the corresponding feasibility space through the projection operator $R^{(p)}$ $[R^{(p)}(\widetilde{x}, \widetilde{y}, \widetilde{z}; t) = \mathbb{R}\{F^{(p)}(\widetilde{x}, \widetilde{y}, \widetilde{z}; t), F^{des}(\widetilde{x}, \widetilde{y}, \widetilde{z}; t)\}]$

$$R^{(p)}(\widetilde{x}, \widetilde{y}, \widetilde{z}; t) = \begin{cases} F^{des}(\widetilde{x}, \widetilde{y}, \widetilde{z}; t), & if\ F^{(p)}(\widetilde{x}, \widetilde{y}, \widetilde{z}; t) < F^{des}(\widetilde{x}, \widetilde{y}, \widetilde{z}; t) \\ F^{(p)}(\widetilde{x}, \widetilde{y}, \widetilde{z}; t), & \text{otherwise.} \end{cases} \qquad (15)$$

The QIPM convergence is checked and the iterations are stopped if either $p = P$ or if the index $\Xi^{(p)}(t)$ ($\Xi^{(p)}(t) \triangleq (\int_{\Psi_{obs}} |R^{(p)}(\widetilde{x}, \widetilde{y}, \widetilde{z}; t) - F^{(p)}(\widetilde{x}, \widetilde{y}, \widetilde{z}; t)| \mathrm{d}\widetilde{x}\mathrm{d}\widetilde{y}\mathrm{d}\widetilde{z} / \int_{\Psi_{obs}} |F^{(p)}(\widetilde{x}, \widetilde{y}, \widetilde{z}; t)| \mathrm{d}\widetilde{x}\mathrm{d}\widetilde{y}\mathrm{d}\widetilde{z})$) complies with the convergence condition $\Xi^{(p)}(t) \leq \Xi^{th}$. If this holds true, the reference current is set to the pth estimate, $\overline{J}^{opt} = \overline{J}^{(p)}$. Otherwise, the minimum norm current, $\overline{J}^{(p)}_{MN}$, corresponding to $R^{(p)}(\widetilde{x}, \widetilde{y}, \widetilde{z}; t)$ is retrieved by means of the truncated singular value decomposition [5], [21]

$$\overline{J}^{(p)}_{MN} = \mathbb{F}^{-1}\left\{\mathbb{H}^{-1}\left\{R^{(p)}(\widetilde{x}, \widetilde{y}, \widetilde{z}; t)\right\}\right\}. \tag{16}$$

The quantization of the minimum norm current is subsequently carried out by approximating it with the closest element of $\mathcal{C}$ ($\overline{J}^{(p+1)} \approx \overline{J}^{(p)}_{MN}$, $\overline{J}^{(p+1)} \in \mathcal{C}$). More in detail, the amplitude and phase coefficients of $\overline{J}^{(p+1)}$ are determined by minimizing the mismatch cost function

$$\rho(\alpha_{mn}(t),\ \chi_{mn}(t)) = \left\{ \frac{\left\| \sum_{m=1}^{M} \sum_{n=1}^{N} \alpha_{mn}(t) \exp[j\chi_{mn}(t)] \Omega_{mn}(x, y) \widehat{\imath} - \overline{J}^{(p)}_{MN} \right\|^2}{\left\| \overline{J}^{(p)}_{MN} \right\|^2} \right\} \tag{17}$$

with $\| \cdot \|$ being the ℓ_2 norm [i.e., $(\alpha^{(p+1)}_{mn}(t),\ \chi^{(p+1)}_{mn}(t)) = \arg\min^{\alpha_{mn}(t)\in\mathcal{A}}_{\chi_{mn}(t)\in\mathcal{X}}\{\rho(\alpha_{mn}(t),\ \chi_{mn}(t))\}$]; they are then substituted in (14) to yield $\overline{J}^{(p+1)}$. The iteration index is then updated ($p \leftarrow p + 1$), and the entire QIPM process is restarted from the footprint pattern computation.

It is worth pointing out that, unlike state-of-the-art approaches [5], [6], the operation in (17) outputs an estimated current $\overline{J}^{(p+1)}$ that fulfills the feasibility condition. This guarantees that the current distribution determined at the convergence, $\overline{J}^{opt}$, can be implemented with a 1RP-EMS layout.

B. 1RP-EMS Configuration Method

By following the guidelines in [5], but here customized to a binary control problem, an SbD-based optimization is carried out to identify the 1RP-EMS discrete microscale status $\mathcal{S}^{opt}(t)$ of $M \times N$ binary entries. Toward this end, a set of L trial 1RP-EMS configurations

$$\langle \mathcal{S}(t) \rangle \triangleq \{\mathcal{S}_l(t);\ l = 1, \ldots, L\} \tag{18}$$

is iteratively processed until either the number of SbD iterations reaches the maximum value I ($i = I$, with i being the iteration index), or the feasible reference current distribution $\overline{J}^{opt}$, computed in Section III-A, is matched (13) [i.e., $\psi(\mathcal{S}^{opt}(t)) \leq \psi^{th}$, $\mathcal{S}^{opt}(t) = \arg(\min_{l,i}[\psi(\mathcal{S}^{(i)}_l(t))])$, with ψ^{th} being a user-defined convergence threshold].

Starting from a random initial configuration, $\langle \mathcal{S}^{(i)}(t) \rangle_{i=0}$, each ith ($i = 1, \ldots, I$) iteration consists of the following operations.

1) *1RP-EMS Surrogate Modeling:* The set of L *microscale* electric/magnetic surface susceptibility vectors, $\langle \mathcal{K}^{(i)}(t) \rangle$ ($\langle \mathcal{K}(t) \rangle \triangleq \{\mathcal{K}_l(t);\ l = 1, \ldots, L\}$), is predicted with an AI-based technique, featuring an *ordinary Kriging* implementation, according to the most recent trends in the surrogate modeling of wave manipulating devices [24], [33]. For each lth entry of $\langle \mathcal{K}^{(i)}(t) \rangle$, the diagonal tensor of the electric/magnetic local surface susceptibility of the (m, n)th ($m = 1, \ldots, M$; $n = 1, \ldots, N$) meta-atom, $\overline{\overline{K}}_{mn}(t)$, is approximated with its DT, $\overline{\overline{K}}_{mn}(t) \approx \overline{\overline{K}}^{DT}_{mn}(t)$ ($\overline{\overline{K}}^{DT}_{mn}(t) \triangleq \mathbb{K}^{DT}\{\mathbf{g};\ s_{mn}(t)\}$), which is off-line trained starting from V full-wave evaluations of the meta-atom response $\{[\mathbf{g}_v,\ s^v_{mn}(t); \mathbb{K}\{\mathbf{g}_v;\ s^v_{mn}(t)\}];\ v = 1, \ldots, V\}$ [24], [33].
2) *Surface Current Computation:* The distribution of the surface current $\overline{J}_l(x, y; t)$ induced on the lth ($l = 1, \ldots, L$) 1RP-EMS, which is modeled with the surrogate susceptibility vector $\mathcal{K}^{DT}_l(t)$, is computed by setting $\overline{\overline{K}}_{mn}(t) = \overline{\overline{K}}^{DT}_{mn}(t)$ in (4).
3) *Surface Current Fitness Evaluation:* The mismatch between $\overline{J}^{(i)}_l$ ($l = 1, \ldots, L$) and $\overline{J}^{opt}$ is quantified by calculating the value of the microscale cost function (13), $\psi(\mathcal{S}^{(i)}_l(t))$.
4) *Guess Current Update* A new set of 1RP-EMS states, $\langle \mathcal{S}^{(i+1)}(t) \rangle$, is generated by applying the genetic-algorithm (GA) operators [34] to the previous guesses, $\langle \mathcal{S}^{(i)}(t) \rangle$, according their fitness values, $\langle \psi^{(i)}(t) \rangle$ ($\langle \psi^{(i)}(t) \rangle \triangleq \{\psi(\mathcal{S}^{(i)}_l(t));\ l = 1, \ldots, L\}$). Unlike [5] and [6], a GA-based optimization is performed due to the binary DoFs of the problem at hand.

The flowchart of the overall proposed methodology is reported in Fig. 2 for completeness.

IV. Numerical Results

This section is aimed at illustrating the synthesis process of 1RP-EMSs described in Section III and at demonstrating its effectiveness and potentialities. Toward this end, the design of the single-bit meta-atom is first presented along with the full-wave validation of its properties (see Section IV-A). Afterward, the 1RP-EMS control is assessed through a selected set of numerical experiments (see Section IV-B). For the full-wave modeling of both the meta-atom and the finite 1RP-EMS layouts, the *Ansys HFSS* [35] EM simulator has been used.

A. Single-Bit Meta-Atom Design and Validation

Since a key objective of this work is to prove that it is possible to achieve advanced beam shaping properties with minimum-complexity RP-EMSs, the design of the single-bit meta-atom has been carried out according to Section II-A by also taking into account the following constraints: 1) the meta-atom features a single-layer geometry to minimize the fabrication complexity; 2) the single-bit ($B = 1$) reconfigurability of the RP-EMS unit cell is obtained by applying a single bias voltage; 3) the shape of the layout of the printed cell is very regular to keep its EM behavior independent on the accuracy of the fabrication process; and 4) the 1RP-EMS structure works whatever the polarization of the incident field.

The unit cell in [36] has been then considered as a reference model. It consists of a simple square patch (see Fig. 3) with two edges connected to the ground plane through two p-i-n diodes [green rectangles; see Fig. 3(a)] and two vias [yellow circles; see Fig. 3(a)]. By applying a bias voltage at the center of the patch, the diodes can be either both set to the "ON" [$s_{mn}(t) = 1$] or both to the "OFF" [$s_{mn}(t) = 0$] states to implement the single-bit-per-atom reconfigurability.

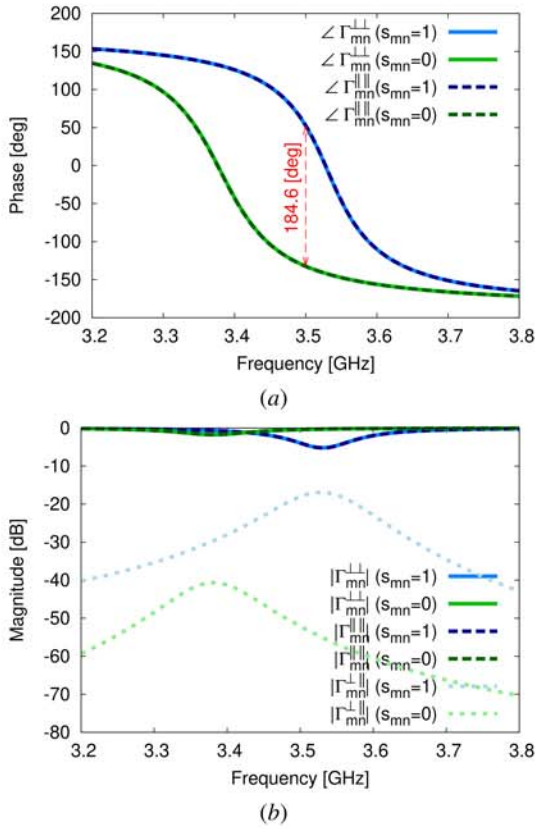

Fig. 4. *1RP-EMS design*—plots of (a) phase and (b) magnitude of the TE/TM components of the local reflection tensor $\overline{\overline{\Gamma}}_{mn}$ versus the frequency in correspondence with the "ON" ($s_{mn} = 1$) and the "OFF" ($s_{mn} = 0$) states.

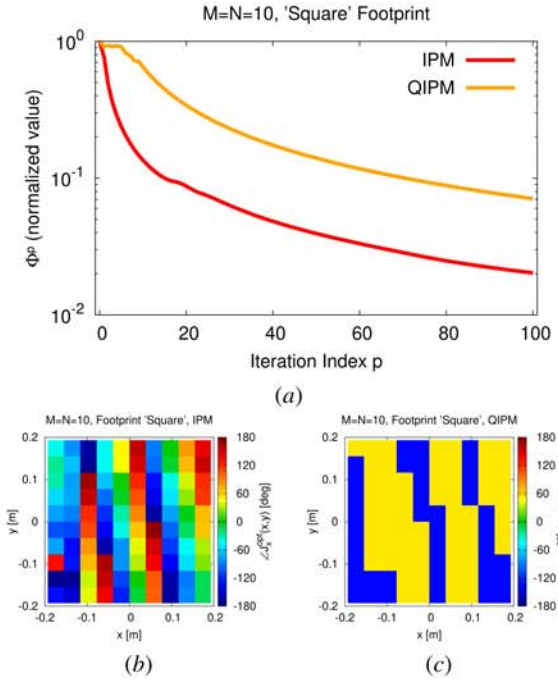

Fig. 5. *1RP-EMS control* (*"square" footprint*: $M = N = 10$, $d = 5$ [m], and $P = 10^2$)—behavior of (a) macroscale cost $\Phi^{(p)}$ versus the iteration index ($p = 1, \ldots, P$) and plot of (b) and (c) phase of the reference current, $\{\overline{J}^{opt}(x_m, y_n; t)$; $(m = 1, \ldots, M;\ n = 1, \ldots, N)\}$, synthesized with (b) IPM, $\overline{J}^{opt}_{IPM}$, and (c) QIPM, $\overline{J}^{opt}_{QIPM}$.

To operate at the central frequency of the sub-6 GHz n78-band [37] (i.e., $f_0 = 3.5$ GHz), such a reference model

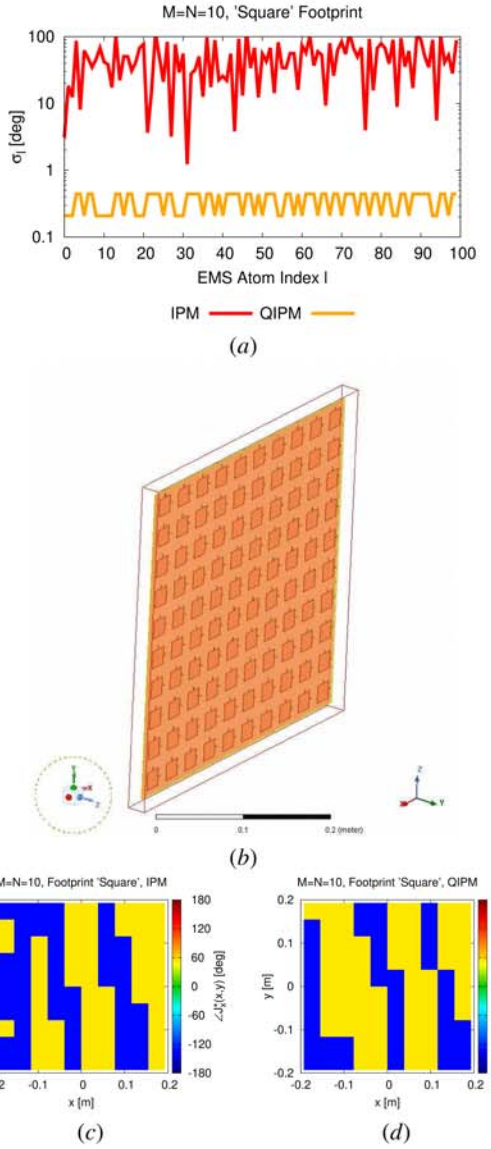

Fig. 6. *1RP-EMS control* (*"square" footprint*: $M = N = 10$ and $d = 5$ [m])—plots of (a) distribution of the local error σ_ℓ [$\ell = n + N \times (m-1)$ $(m = 1, \ldots, M;\ n = 1, \ldots, N)$] and of (c) and (d) phase of the current, $\{\overline{J}^*(x_m, y_n; t)$ $(m = 1, \ldots, M;\ n = 1, \ldots, N)\}$, generated by the 1RP-EMS (b) configured with (c) IPM-based approach, $\overline{J}^*_{IPM}$, or (d) QIPM one, $\overline{J}^*_{QIPM}$.

has been tuned by considering a Rogers RO4350 ($\varepsilon_r = 3.66$ and $\tan\delta = 4.0 \times 10^{-3}$) substrate with thickness of 1.524×10^{-3} m that includes 3.5×10^{-5} m-thick metalizations and the MACOM MADP-000907-14020 diodes. The values of the $\mathbf{g}^{opt}$ entries are listed in Table I, while the CAD models of the unit cell and of the switching device are shown in Fig. 3(b) and (c), respectively.

The reflection performance of the optimized meta-atom is illustrated in Fig. 3 for the broadside incidence. More in detail, the plots of the phase [see Fig. 4(a)] and the magnitude [see Fig. 4(b)] of the TE/TM components of the local reflection tensor $\overline{\overline{\Gamma}}_{mn}(t)$ indicate that such a meta-atom supports a $\approx$180° phase difference between the "ON" [$s_{mn}(t) = 1$] and the "OFF" [$s_{mn}(t) = 0$] states at f_0 [see Fig. 4(a)]. Thanks to the symmetry of the layout, the arising unit cell is insensitive to the polarization [see Fig. 3(a)]. Moreover, the losses are limited [<4 dB; see Fig. 4(b)], and the cross-polarization level

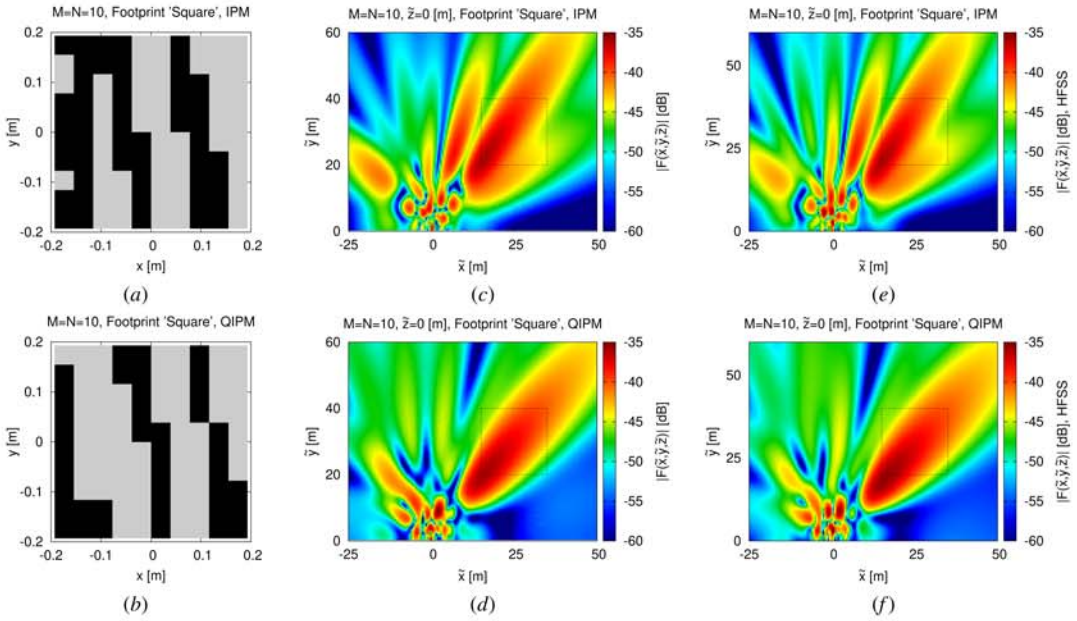

Fig. 7. *1RP-EMS control ("square" footprint*: $M = N = 10$ and $d = 5$ [m])—plots of (a) and (b) ON/OFF states and the corresponding (c) and (d) analytically computed and (e) and (f) HFSS-simulated footprint patterns of (a) IPM and (b) QIPM 1RP-EMS.

TABLE I

1RP-EMS Design—GEOMETRICAL DESCRIPTORS

Parameter	*Value [m]*
$g_1^{opt} = g_2^{opt}$	3.854×10^{-2}
$g_3^{opt} = g_4^{opt}$	2.191×10^{-2}
$g_5^{opt} = g_{11}^{opt}$	1.616×10^{-4}
$g_6^{opt} = g_{12}^{opt}$	2.488×10^{-3}
$g_7^{opt} = g_{13}^{opt}$	3.300×10^{-4}
$g_8^{opt} = g_{14}^{opt}$	1.777×10^{-3}
$g_9^{opt} = g_{15}^{opt}$	2.000×10^{-4}
$g_{10}^{opt} = g_{16}^{opt}$	6.000×10^{-4}

is low [<-18 dB; see Fig. 4(b)] within the whole frequency band.

It is finally worthwhile to remark that, while the successive control step (see Section II-B) has been performed in this article with the single-bit cell in Fig. 3, the proposed approach for configuring the 1RP-EMS can be adopted regardless of the working frequency, the number of bits per cell, B, and the meta-atom complexity [38].

B. Single-Bit RP-EMS Control

To assess the features and the potentialities of the 1RP-EMS control method in Sections III-A and III-B, different EMS apertures and target radiation performance have been analyzed by considering an SEME scenario where a 1RP-EMS is placed at $d = 5$ m the ground (see Fig. 1), it is illuminated by a base station located along the EMS broadside direction [i.e., $(\theta^{inc}, \varphi^{inc}) = (0, 0)^\circ \rightarrow \widehat{\mathbf{e}}_\perp = \widehat{\mathbf{y}}$ and $\widehat{\mathbf{e}}_\parallel = \widehat{\mathbf{x}}$], and it is equipped with a slant $+45^\circ$ linearly polarized antenna (i.e., $E_\perp^{inc} = E_\parallel^{inc} = 1$). As for the calibration setup of the 1RP-EMS control, the following values have been chosen according to the guidelines in [5] and [24]: $V = 2 \times 10^4$, $P = 10^2$, $L = 20$, $\Xi^{th} = 10^{-4}$, $\psi^{th} = 10^{-3}$, and $I = 10^4$.

1) Square Footprint: The first experiment is aimed at configuring an $M \times N = 10 \times 10$ 1RP-EMS to maximize the reflected power in a square Ψ_{cov} of size 10×10 m^2 located in the global coordinate system (see Fig. 1) at $(\widetilde{x}, \widetilde{y}, \widetilde{z}) = (25, 30, 0)$ m, which corresponds to set the desired footprint

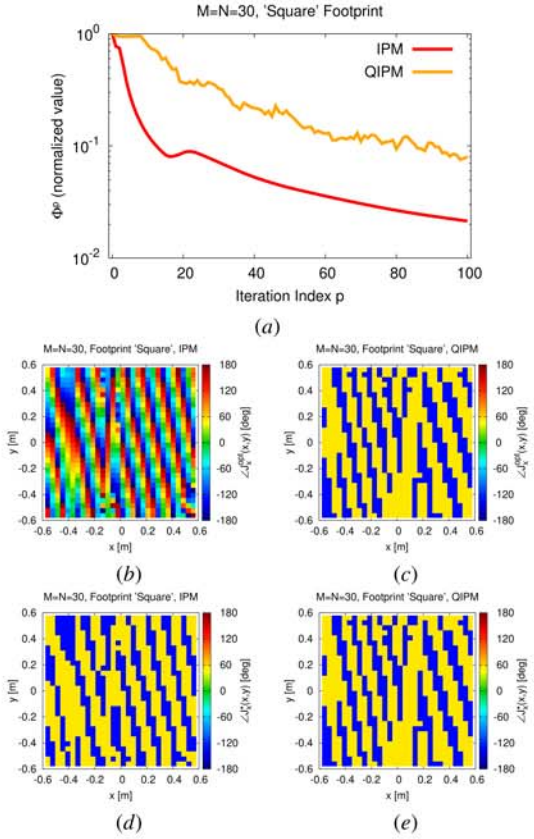

Fig. 8. *1RP-EMS control ("square" footprint*: $M = N = 30$ and $P = 10^2$)—behavior of (a) macroscale cost $\Phi^{(p)}$ versus the iteration index ($p = 1, \ldots, P$) and plots of the phase of (b) and (c) reference current, $\{\overline{J}^{opt}(x_m, y_n; t)$ $(m = 1, \ldots, M;\ n = 1, \ldots, N)\}$ and of (d) and (e) current, $\{\overline{J}^{*}(x_m, y_n; t)$ $(m = 1, \ldots, M;\ n = 1, \ldots, N)\}$, generated by the configured 1RP-EMS in [see Fig. 9(a)] when applying (b) and (d) IPM-based approach or (c) and (e) QIPM one.

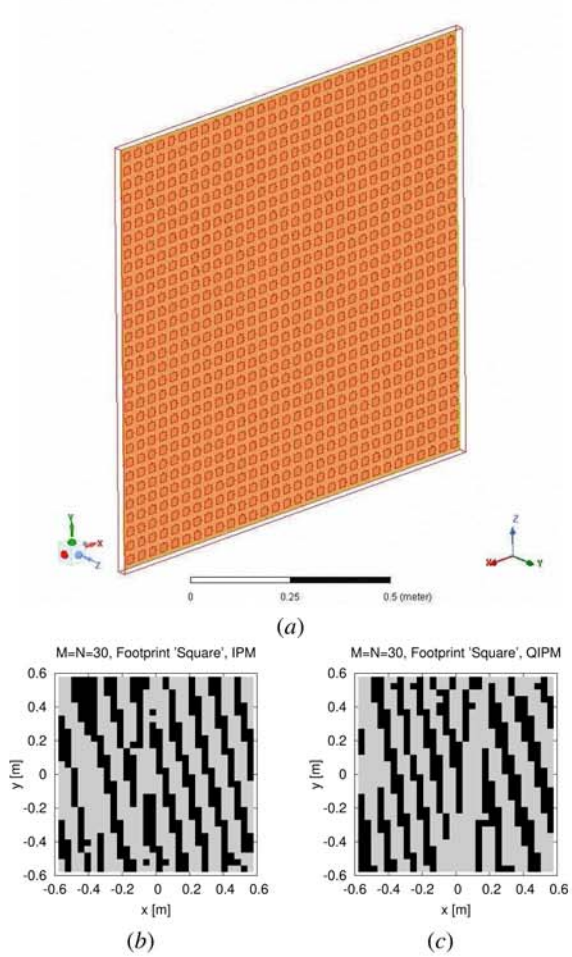

Fig. 9. *1RP-EMS control ("square" footprint*: $M = N = 30$ and $d = 5$ [m])—plot of (a) 3-D model of the RP-EMS and map of (b) and (c) ON/OFF states of the 1RP-EMS yielded with (b) IPM, $\mathcal{S}_{IPM}^{opt}$, and (d) QIPM, $\mathcal{S}_{QIPM}^{opt}$, approaches.

pattern as follows:

$$F^{des}(\widetilde{x},\widetilde{y},\widetilde{z};t)=\begin{cases}-10\,\text{dB}, & (\widetilde{x},\widetilde{y},\widetilde{z})\in\Psi_{cov}\\ -50\,\text{dB}, & (\widetilde{x},\widetilde{y},\widetilde{z})\notin\Psi_{cov}\end{cases} \tag{19}$$

with $t = T = 1$.

Fig. 5(a) shows the behavior of the macroscale cost function (10) $\Phi^{(p)}$ during the QIPM-based process ($p = 1, \ldots, P$) for the synthesis of the reference surface current in comparison with that of the IPM technique [5]. As expected, the QIPM does not outperform the IPM in terms of footprint pattern matching (i.e., $\Phi_{QIPM}^{(p)} > \Phi_{IPM}^{(p)}$, $p = 1, \ldots, P$) since the former is a constrained version of the latter owing to the binary nature of the meta-atoms and the quantization of the arising current distribution. Indeed, unlike the smoothly varying phase distribution of the IPM [see Fig. 5(b)] that ignores any limitation to the phase control, the profile of the phase distribution of the QIPM current turns out to be binarized [see Fig. 5(c)]. Such an apparent drawback [see Fig. 5(a)] is actually a fundamental advantage of the QIPM when dealing with the subsequent SbD-driven microscale state optimization (see Fig. 6). As a matter of fact, the plot of the local error $\sigma(m,n)$ ($m = 1, \ldots, M$; $n = 1, \ldots, N$)

$$\sigma(m,n;t)\triangleq\angle\overline{J}^{opt}(x_m,y_n;t)-\angle\overline{J}^{*}(x_m,y_n;t) \tag{20}$$

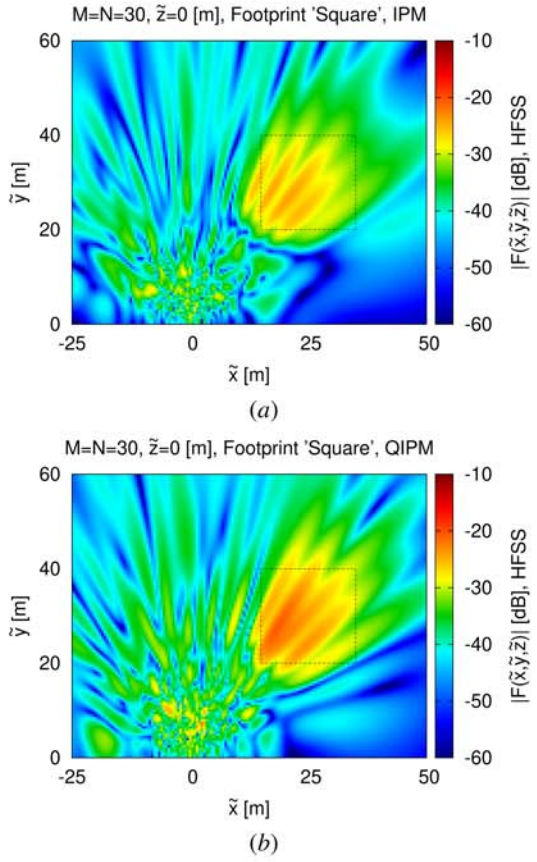

Fig. 10. *1RP-EMS control ("square" footprint*: $M = N = 30$ and $d = 5$ [m])—plots of the HFSS-simulated footprint pattern radiated by (a) IPM and (b) QIPM 1RP-EMS.

$[\overline{J}^{*}(x,y;t)=\mathbb{G}\{\mathbb{K}\{\mathbf{g};s_{mn}^{opt}(t)\};\overline{E}^{inc}(x,y,0;t)\}]$ in approximating the phase of the reference current distribution with the 1RP-EMS in Fig. 6(b) points out that it is more difficult to match the IPM-synthesized one, while the mismatch reduces in the QIPM case [see Fig. 6(a)] (i.e., $3 \leq \sigma^{IPM}(m,n) \leq 121°$ versus $0.2 \leq \sigma^{QIPM}(m,n) \leq 0.45°$), as one can visually notice by comparing the phase profiles of the reference and the synthesized currents $[\overline{J}_{IPM}^{opt}(x,y;t)$—Fig. 5(b)—versus $\overline{J}_{IPM}^{*}(x,y;t)$—Fig. 6(c); $\overline{J}_{QIPM}^{opt}(x,y;t)$—Fig. 5(c)—versus $\overline{J}_{QIPM}^{*}(x,y;t)$—Fig. 6(d)].

In order to analyze the impact of those results on the coverage performance, the plots of the analytically computed [see Fig. 7(c) and (d)] and the HFSS-simulated [see Fig.7(e) and (f)] footprint patterns generated by the IPM [see Fig. 7(a)] and the QIPM [see Fig. 7(b)] 1RP-EMS in an observation region Ψ_{obs} of 75×60 [m^2] located in front of the RP-EMS are reported.

Despite the relatively small EMS aperture and its very limited (binary) reconfiguration capabilities, the QIPM configuration [see Fig. 7(b)] of the 1RP-EMS focuses the reflected beam in the desired coverage region Ψ_{cov} (i.e., along a non-Snell direction) better than the IPM one [see Fig. 7(a)] with a lower number of sidelobes [see Fig. 7(c) versus Fig. 7(d)]. Moreover, the close fitting between analytically computed [see Fig. 7(c) and (d)] and HFSS-simulated [see Fig. 7(e) and (f)] patterns proves the accuracy of the analytic prediction of the reflection/focusing properties of the 1RP-EMS layout despite the finite EMS aperture and the intrinsic approximations of

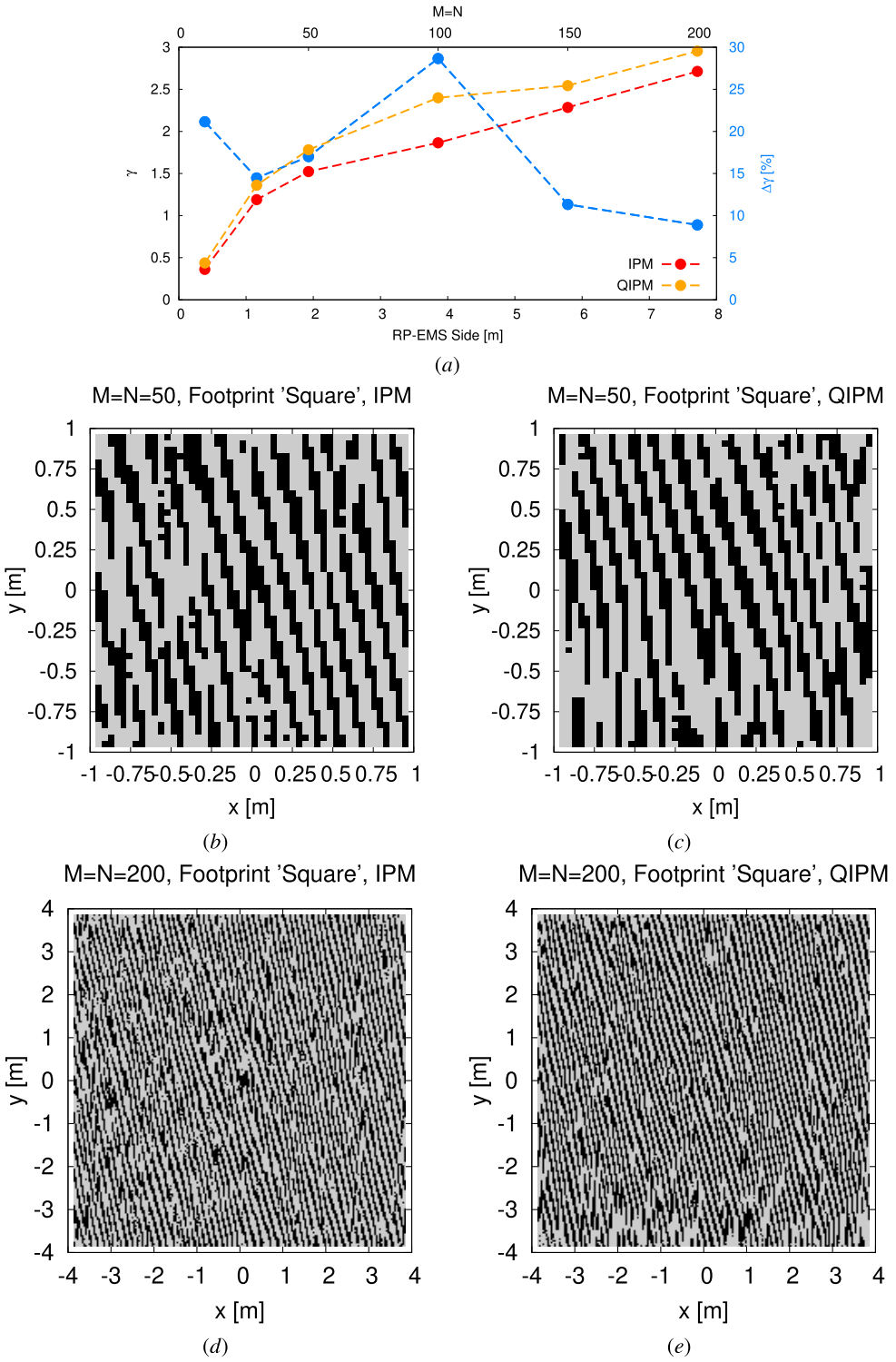

Fig. 11. *1RP-EMS control ("square" footprint*: $d = 5$ [m])—behaviors of (a) total, γ, and the relative, $\Delta\gamma$, coverage indexes versus the 1RP-EMS size and maps of (b)–(e) ON/OFF configurations of the 1RP-EMS synthesized with (b) and (d) IPM and (c) and (e) QIPM when (b) and (c) $M \times N = 50 \times 50$ and (d) and (e) $M \times N = 200 \times 200$.

the analytical model. Such an outcome, which is also in line with the conclusions drawn for the SP-EMS case [5], [6], further confirms the reliability of the proposed multiscale design without the need for recurring to expensive full-wave simulations in the online synthesis process and its effectiveness to control the macroscale wave manipulation properties of 1RP-EMSs.

When increasing the EMS size Ψ_{EMS} ($M = N = 10 \rightarrow M = N = 30$) by keeping the same target coverage region Ψ_{obs} and footprint requirements (19), similar considerations to those of the first numerical experiment hold true. For the sake of completeness and analogously to the $M \times N = 10 \times 10$ case, Figs. 8–10 illustrate the process for configuring the 1RP-EMS by also comparing the QIPM-based approach

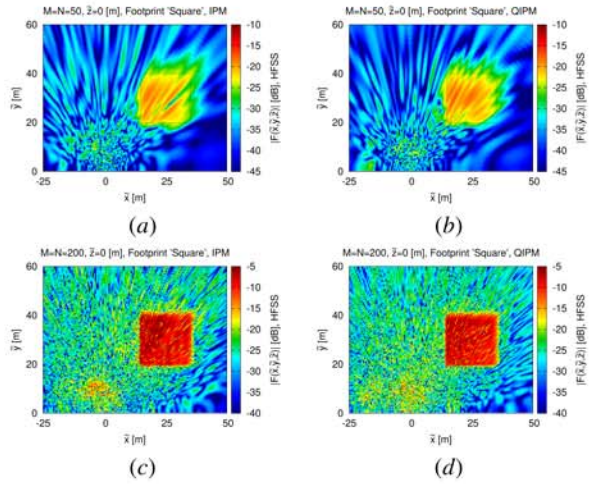

Fig. 12. *1RP-EMS control ("square" footprint*: $d = 5$ [m])—plots of the HFSS-simulated footprint pattern radiated by (a) and (c) IPM and (b) and (d) QIPM 1RP-EMS when (a) and (b) $M \times N = 50 \times 50$ and (c) and (d) $M \times N = 200 \times 200$.

with the IPM one. Fig. 7 deals with the current synthesis, while Fig. 9 is concerned with the configuration of the 1RP-EMS, and Fig. 10 gives the radiated footprint patterns. More in detail, Fig. 8(a) shows the iterative QIPM/IPM minimization of the macroscale cost function (10) to define the reference (phase) current profiles in Fig. 8(b) and (c) that are approximated [see Fig. 8(d) and (e)] by the SbD-optimized setups [see Fig. 9(b) and (c)] of the 1RP-EMS in Fig.9(a) to afford the footprint patterns in Fig. 10(a) and (b). Once again, the constrained nature of the QIPM solution [see Fig. 8(c)] allows one to better configure [see Fig. 9(c)] the 1RP-EMS [see Fig. 9(a)] for more faithfully fulfilling the target coverage [see Fig. 10(b)]. The improved focusing performance of the QIPM-based control is quantified by the value of the *footprint coverage index* γ

$$\gamma \triangleq \frac{W_{cov}}{W_{ext}} \tag{21}$$

where $W_\Psi \triangleq (1/2\eta_0) \int_\Psi F(\tilde{x}, \tilde{y}, \tilde{z}; t) \mathrm{d}\tilde{x}\mathrm{d}\tilde{y}\mathrm{d}\tilde{z}$ is the power reflected in the Ψ region and $\Psi_{ext} = \Psi_{obs} - \Psi_{cov}$, which is equal to $\gamma^{QIPM} \approx 4.3 \times 10^{-1}$, while $\gamma^{IPM} \approx 3.6 \times 10^{-1}$ [see Fig. 11(a)].

In order to give the interested readers a more exhaustive picture of the advantages of using the QIPM approach instead of the IPM one when dealing with discrete RP-EMSs, Fig. 11(a) compares the behavior of γ^{IPM} and γ^{QIPM} versus the size of the 1RP-EMS aperture by reporting the relative index $\Delta\gamma$ ($\Delta\gamma \triangleq (\gamma^{QIPM} - \gamma^{IPM}/\gamma^{IPM})$) as well. As it can be observed, the proposed method (see Section III) always determines a configuration of the same 1RP-EMS that better focuses the reflected power toward the coverage region Ψ_{cov} (i.e., $\gamma^{QIPM} > \gamma^{IPM}$) with a nonnegligible improvement of the power efficiency [i.e., $8\% \leq \Delta\gamma \leq 30\%$; see Fig. 11(a)] also when wide apertures are at hand.

For illustrative purposes, the synthesized ON/OFF configurations of the 1RP-EMS [see Fig. 11(b)–(e)] and the corresponding footprint patterns (see Fig. 12) when $M \times N = 50 \times 50$ [see Figs. 11(b) and (c) and 12(a) and (b)] and $M \times N = 200 \times 200$ [see Figs. 11(d) and (e) and 12(c) and (d)] are reported as well. Despite the exponentially increasing

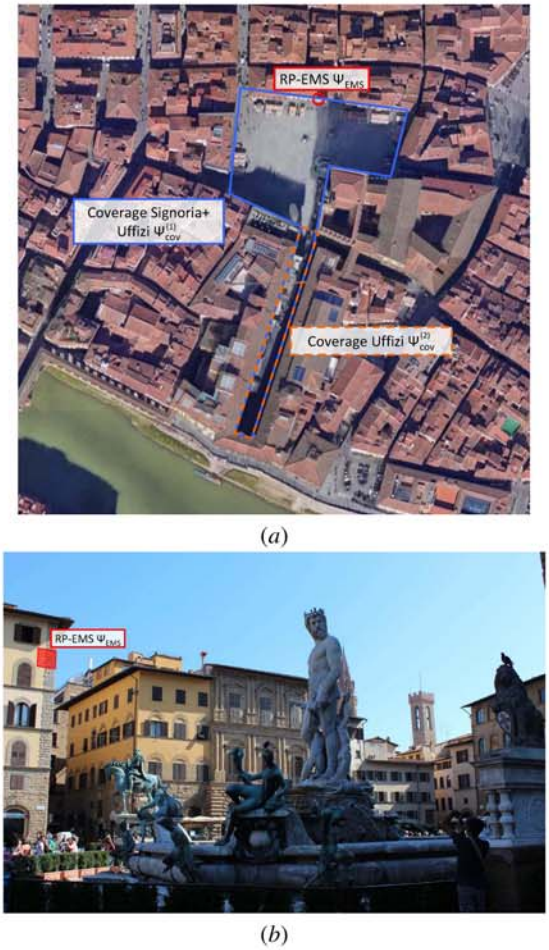

Fig. 13. *1RP-EMS control ("Signoria + Uffizi" and "Uffizi" footprints*: $M = N = 30$ and $d = 15$ [m])—view of (a) scenario and (b) location of the 1RP-EMS.

complexity of the optimization problem at hand (12) owing to the widening of the discrete solution space [i.e., 8.4×10^{270} ($M \times N = 30 \times 30$), 3.7×10^{752} ($M \times N = 50 \times 50$), and 1.5×10^{12041} ($M \times N = 200 \times 200$) binary configurations, $\mathcal{S}(t)$], the control method in Section III-B turns out to be very effective in finding the optimal 1RP-EMS configuration $\mathcal{S}^{opt}(t)\rfloor_{t=T=1}$ whatever the size of Ψ_{EMS}, thus improving the beam focusing capabilities of the 1RP-EMS [see Fig. 11(a)] by fully exploiting the aperture enlargement [see Fig. 7(d) ($M \times N = 10 \times 10$) versus Fig. 10(b) ($M \times N = 30 \times 30$) versus Fig. 12(b) ($M \times N = 50 \times 50$) versus Fig. 12(d) ($M \times N = 200 \times 200$)].

2) "Signoria + Uffizi" and "Uffizi" Footprints: The next numerical experiment is concerned with the case of a *multistatic reconfigurability* ($t \in \{t_1, t_2\}$; $t = 1, \ldots, T$), and it deals with the installation of a 1RP-EMS to alternatively target the wireless coverage of the Piazza della Signoria or Piazzale degli Uffizi in Florence (Italy) (i.e., one of the most frequented urban areas in Europe) that consist of an L-shaped wider square, $\Psi_{cov}^{(1)}$, and a narrow adjacent site, $\Psi_{cov}^{(2)}$, where the entrance to the Uffizi museum is located [see Fig. 13(a)]. The 1RP-EMS, which has been assumed to be placed at $d = 15$ m on the building in Fig. 13(b), is requested to switch between the "Signoria + Uffizi" coverage (i.e., $F^{des}(\tilde{x}, \tilde{y}, \tilde{z}; t)\rfloor_{t=t_1}$ as in (19) by setting $\Psi_{cov} = \Psi_{cov}^{(1)}$) and the "Uffizi" coverage (i.e., $F^{des}(\tilde{x}, \tilde{y}, \tilde{z}; t)\rfloor_{t=t_2}$ as in (19) by setting $\Psi_{cov} = \Psi_{cov}^{(2)}$).

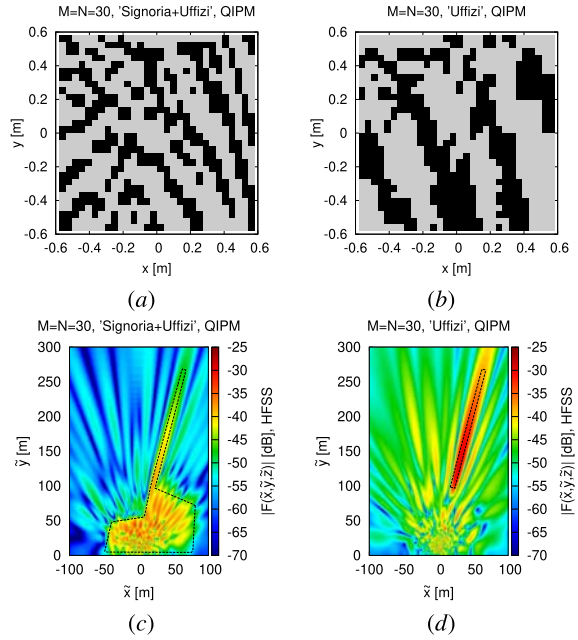

Fig. 14. *1RP-EMS control ("Signoria + Uffizi" and "Uffizi" footprints*: $M = N = 30$ and $d = 15$ [m]; QIPM)—plots of (a) and (b) ON/OFF states of the 1RP-EMS and (c) and (d) corresponding HFSS-simulated footprint patterns when focusing on (a) and (c) "Signoria + Uffizi" area and (b) and (d) "Uffizi" area.

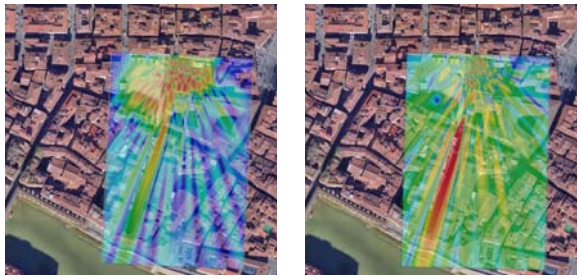

Fig. 15. *1RP-EMS control ("Signoria + Uffizi" and "Uffizi" footprints*: $M = N = 30$ and $d = 15$ [m]; QIPM)—coverage check when dealing with (a) "Signoria + Uffizi" and (b) "Uffizi" coverage scenarios.

The configurations of the ON/OFF states of an $M \times N = 30 \times 30$ layout (i.e., $\Psi_{EMS} \approx 1.3 \times 1.3$ [m^2]), which affords the $T = 2$ footprint patterns in Fig. 14(c) and (d), are reported in Fig. 14(a) and (b). As it can be observed, there are few similarities between the two control maps, $\mathcal{S}^{opt}(t)\rfloor_{t=t_1}$ and $\mathcal{S}^{opt}(t)\rfloor_{t=t_2}$, even though the coverage regions at hand, $\{\Psi_{cov}^{(c)}, (c = 1, \ldots, C;\ C = 2)\}$, partially overlap [see Fig. 13(a)]. Such a behavior is not unexpected due to both the strong nonlinearity of the control problem at hand (12) and the binary nature of the control DoFs.

Concerning the distribution of the radiated power pattern, Fig. 15 confirms the effectiveness of the synthesized layouts in fulfilling the coverage requirements, the footprint patterns faithfully overlapping the area of interest, despite the irregular geometries of the regions of interest and the relatively limited number of reconfigurable states [$\leq$1 [Kbit]; see Fig. 9(a)]. On the other hand, it is also worth noticing that, although the wireless coverage of the "Signoria + Uffizi" area, $\Psi_{cov}^{(1)}$, is a more challenging problem than that of the "Uffizi" site, $\Psi_{cov}^{(2)}$, since it requires the 1RP-EMS focuses the reflected power also at very low elevation angles with respect to its location [see Fig. 14(c)], the amount of power reflected by the 1RP-EMS is kept almost unaltered (i.e., $(W_{cov}^{(2)}/W_{cov}^{(1)}) \approx 0.78$).

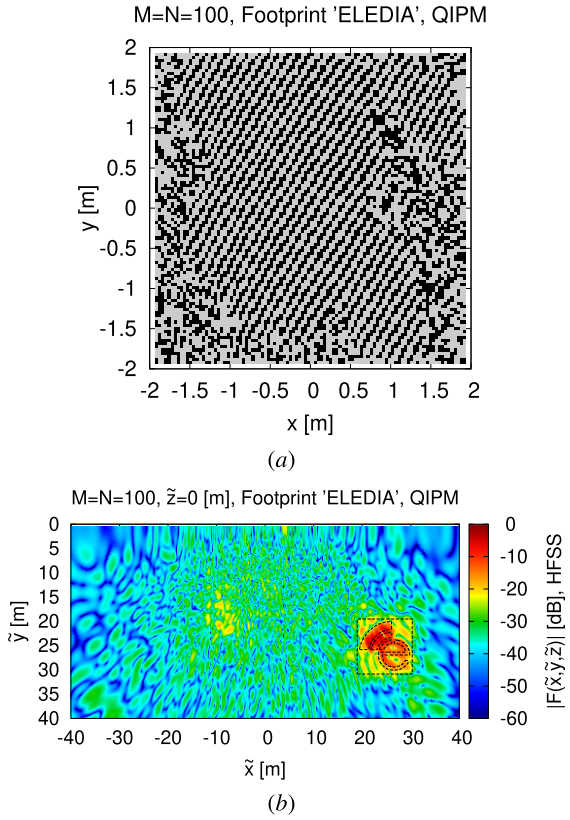

Fig. 16. *1RP-EMS control ("ELEDIA" footprint*: $M = N = 100$ and $d = 15$ [m]; QIPM)—plots of (a) ON/OFF states of the 1RP-EMS and (b) corresponding HFSS-simulated footprint pattern.

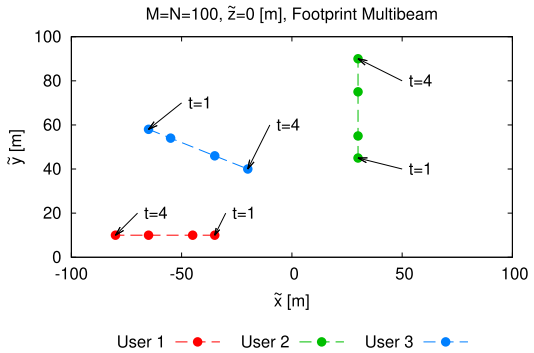

Fig. 17. *1RP-EMS control (multibeam footprint*: $M = N = 100$ and $d = 5$ [m]; QIPM)—users' trajectories.

3) "ELEDIA" Footprint: The ability to afford more elaborated/overconstrained footprints by controlling a 1RP-EMS has been assessed with the synthesis of an $M \times N = 100 \times 100$ 1RP-EMS devoted to manipulating the reflected power for matching the "ELEDIA" logo pattern [see Fig. 16(b)]. The plot of the full-wave simulated footprint pattern, $F^{opt}(\tilde{x}, \tilde{y}, \tilde{z}; t)\rfloor_{t=1}$, in an observation region $\Psi_{obs}^{(c)}$ of extension 80×40 [m^2] [see Fig. 16(b)] proves the reliability of the EMS configuration $\mathcal{S}^{opt}(t)\rfloor_{t=T=1}$ in Fig. 16(a) to match the coverage requirements on a complex region Ψ_{cov}. The readers are suggested to notice that this test case has been already successfully addressed in [5] with SP-EMSs, but, here, the DoFs are far less than those available in the SP-EMS case [5].

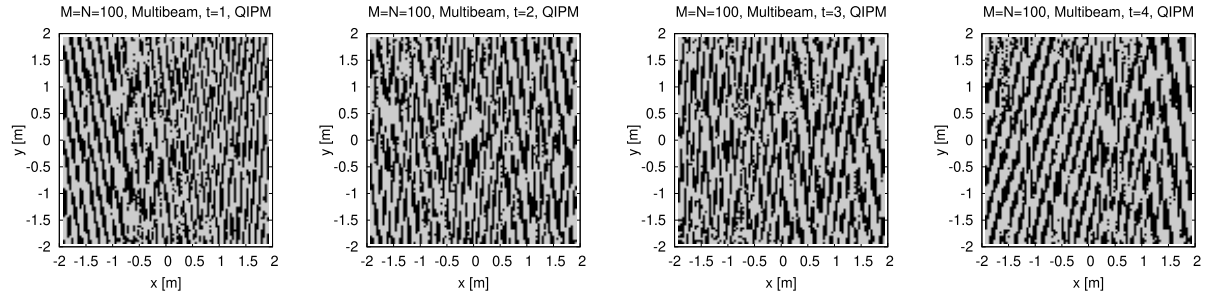

(*a*) (*b*) (*c*) (*d*)

Fig. 18. *1RP-EMS control* (*multibeam footprint*: $M = N = 100$ and $d = 5$ [m]; QIPM)—plots of the ON/OFF states of the 1RP-EMS at (a) $t = 1$, (b) $t = 2$, (c) $t = 3$, and (d) $t = T$ ($T = 4$).

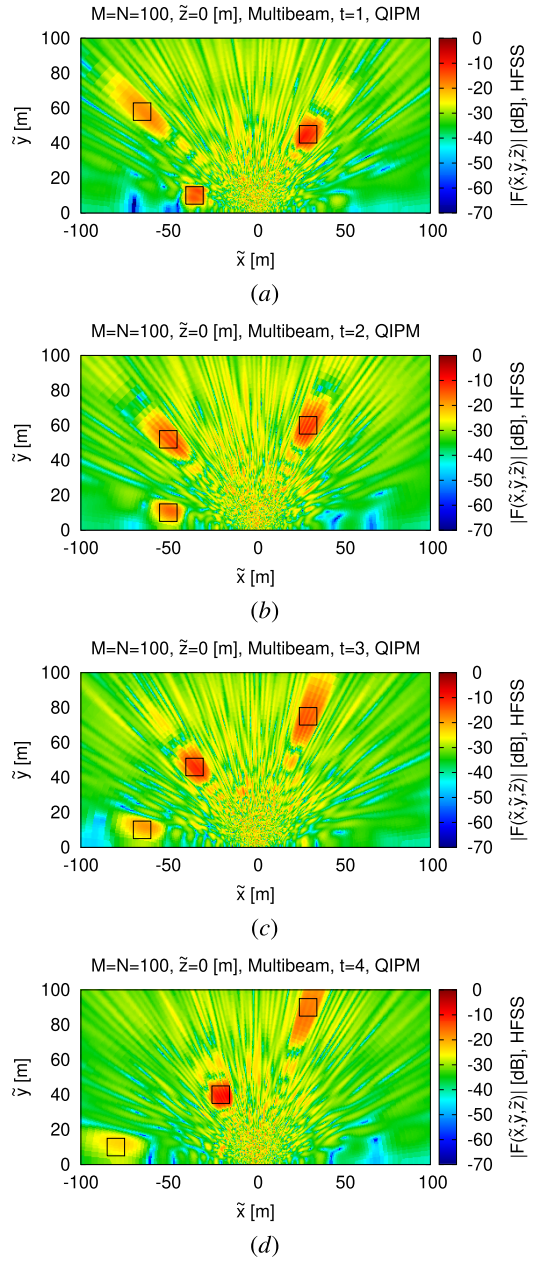

(*a*) (*b*) (*c*) (*d*)

Fig. 19. *1RP-EMS control* (*multibeam footprint*: $M = N = 100$ and $d = 5$ [m]; QIPM)—plots of the 1RP-EMS HFSS-simulated footprint patterns at (a) $t = 1$, (b) $t = 2$, (c) $t = 3$, and (d) $t = T$ ($T = 4$).

4) Dynamic Multibeam Footprint: Finally, the numerical assessment ends with a test on the performance of the proposed 1RP-EMS synthesis method in a scenario that needs a *dynamic multibeam* ($C = 3$) *reconfigurability*. More in detail, the problem at hand is that of $C = 3$ users, each occupying a coverage region $\Psi_{cov}^{(c)}$ ($c = 1, \ldots, C$) of size 10×10 [m^2], which move at different speeds in different directions, as sketched in Fig. 17. By still considering the $M \times N = 100 \times 100$ 1RP-EMS aperture, the plots of the footprint pattern [see Fig. 19(a)–(d)] radiated by the corresponding ON/OFF configuration of the EMS [see Fig. 18(a)–(d)] in $T = 4$ subsequent time instants confirm that such a technological solution fits the users' needs without installing multiple RP-EMSs or using multibit-per-atom reconfiguration schemes.

From a computational perspective and to give some insights on the burden for dynamically managing an EMS-driven wireless planning, let us consider that a tth ($t = 1, \ldots, T$) reconfiguration of the $M \times N = 100 \times 100$ 1RP-EMS for the last scenario (see Fig. 17) required less than 0.2 [s] to a nonoptimized MATLAB implementation of the control algorithm (see Sections III-A and III-B) running on a standard laptop equipped with a single-core 1.6 GHz CPU. Such a quite impressive result has been obtained thanks to the profitable integration of the QIPM strategy (see Section III-A) and the SbD-based binary optimization (see Section III-B). Moreover, to the best of our knowledge on the state-of-the-art literature on EMSs, it turns out that the proposed EMS implementation/control can be properly considered as a suitable candidate/tool for the real-time coverage of time-varying wireless scenarios.

V. Conclusion

An innovative method for the synthesis and control of RP-EMSs has been proposed to deal with layouts based on single-bit meta-atoms able to support advanced propagation manipulation features in SEME scenarios. The introduced technique allows addressing both: 1) the design of the physical layout of the 1RP-EMS structure and 2) its optimal control to match the desired time-varying wireless coverage. Toward this end, the associated multiscale optimization problem has been addressed starting from the design of a meta-atom that features only a single-bit reconfiguration. The control problem has been then addressed by initially computing a discrete-phase current, which radiates a field distribution fitting complex user-defined requirements on the footprint pattern. Then, a digital SbD-based optimization has been carried out to set the binary configuration of the RP-EMS atoms that supports such a reference discrete-phase current.

To the best of our knowledge of the state-of-the-art literature, the main theoretical and methodological advancements of this work include the following:

1) the assessment that RP-EMS architectures featuring single-bit meta-atoms can allow complex wave manipulations (i.e., contoured single/multiple footprint patterns) without the need for continuous phase variations [5], [6];
2) the derivation of an approach for the control of the RP-EMS to afford complex footprint shapes and not only pencil beams [9];
3) the nontrivial extension of the synthesis paradigm, adopted so far to design static reflectarrays and SP-EMSs [5], [6], [21], to minimum-complexity RP-EMSs by deriving a computationally effective reconfiguration method.

From the numerical validation, the following outcomes and accomplishments can be remarked.

1) The QIPM-based approach for the definition of the reference currents significantly improves the coverage efficiency with respect to state-of-the-art techniques [5] regardless of the 1RP-EMS aperture at hand [see Fig. 11(a)].
2) Despite the minimum complexity of the meta-atoms ($B = 1$), the synthesized RP-EMSs feature advanced wave manipulation properties in realistic scenarios (see Fig. 15) and very complex "demonstrative" cases (e.g., Fig. 16).
3) The proposed method turns out to be an enabling tool for multibeam reconfiguration and/or independent user-tracking through 1RP-EMS layouts, therefore demonstrating the feasibility of such relatively inexpensive and low-complexity structures in SEME scenarios requiring adaptive wireless coverage (see Figs. 17–19).

Future works, beyond the scope of this manuscript, will be aimed at assessing the performance of the proposed method when using multibit meta-atoms and/or different meta-atom geometries.

APPENDIX

Expression of $\overline{E}_{mn}(t)$ and $\overline{H}_{mn}(t)$

The surface averaged fields $\overline{E}_{mn}(t)$ and $\overline{H}_{mn}(t)$ can be expressed as [5], [6], [11]

$$\overline{E}_{mn}(t) = \int_{-\frac{M\Delta x}{2}}^{\frac{M\Delta x}{2}} \int_{-\frac{N\Delta y}{2}}^{\frac{N\Delta y}{2}} \Omega_{mn}(x,y) \frac{\left\{\overline{\overline{1}} + \overline{\overline{\Gamma}}_{mn}(t)\right\} \cdot \overline{E}^{inc}(x,y,0)}{2 \times \Delta x \times \Delta y} \mathrm{d}x\mathrm{d}y \tag{22}$$

and

$$\overline{H}_{mn}(t) = \int_{-\frac{M\Delta x}{2}}^{\frac{M\Delta x}{2}} \int_{-\frac{N\Delta y}{2}}^{\frac{N\Delta y}{2}} \Omega_{mn}(x,y) \frac{\left\{\mathbf{k}^{inc} \times \overline{E}^{inc}(x,y,0) + \mathbf{k}^{ref} \times \overline{\overline{\Gamma}}_{mn}(t) \cdot \overline{E}^{inc}(x,y,0)\right\}}{2 \times \Delta x \times \Delta y \times \eta_0 \times k_0} \times \mathrm{d}x\mathrm{d}y \tag{23}$$

respectively, where $\overline{\overline{\Gamma}}_{mn}(t)$ is the local reflection tensor in the (m, n)th cell [5], [6], [11] [$\overline{\overline{\Gamma}}_{mn}(t) = \mathbb{Y}\{\mathbf{g}; s_{mn}(t)\}$] and $\overline{E}^{inc}$ is the incident electric field [32]

$$\overline{E}^{inc}(x,y,z) \triangleq \left(E_{\perp}^{inc}\widehat{\mathbf{e}}_{\perp} + E_{\parallel}^{inc}\widehat{\mathbf{e}}_{\parallel}\right) \exp\left[-j\mathbf{k}^{inc} \cdot (x\widehat{\mathbf{x}} + y\widehat{\mathbf{y}} + z\widehat{z})\right] \tag{24}$$

where $\mathbf{k}^{inc}$ is the incident wave vector ($\mathbf{k}^{inc} \triangleq -k_0[\sin(\theta^{inc})\cos(\varphi^{inc})\widehat{\mathbf{x}} + \sin(\theta^{inc})\sin(\varphi^{inc})\widehat{\mathbf{y}} + \cos(\theta^{inc})\widehat{z}]$), $\mathbf{k}^{ref}$ is the corresponding reflected wave vector according to standard plane wave theory [11], and $\widehat{\mathbf{e}}_{\perp} = (\mathbf{k}^{inc} \times \widehat{\boldsymbol{\nu}}/|\mathbf{k}^{inc} \times \widehat{\boldsymbol{\nu}}|)$ and $\widehat{\mathbf{e}}_{\parallel} = (\widehat{\mathbf{e}}_{\perp} \times \mathbf{k}^{inc}/|\widehat{\mathbf{e}}_{\perp} \times \mathbf{k}^{inc}|)$ are the "perpendicular" and "parallel" unit vectors (i.e., TE and TM modes) [5], [6], [11].

ACKNOWLEDGMENT

Andrea Massa wishes to thank E. Vico for her never-ending inspiration, support, guidance, and help.

REFERENCES

[1] C. Liaskos, S. Nie, A. Tsioliaridou, A. Pitsillides, S. Ioannidis, and I. Akyildiz, "A new wireless communication paradigm through software-controlled metasurfaces," *IEEE Commun. Mag.*, vol. 56, no. 9, pp. 162–169, Sep. 2018.

[2] M. Renzo, "Smart radio environments empowered by reconfigurable AI meta-surfaces: An idea whose time has come," *EURASIP J. Wireless Commun. Netw.*, vol. 129, pp. 1–20, May 2019.

[3] M. Di Renzo *et al.*, "Smart radio environments empowered by reconfigurable intelligent surfaces: How it works, state of research, and the road ahead," *IEEE J. Sel. Areas Commun.*, vol. 38, no. 11, pp. 2450–2525, Nov. 2020.

[4] A. Massa *et al.*, "Designing smart electromagnetic environments for next-generation wireless communications," *Telecom*, vol. 2, no. 2, pp. 213–221, May 2021.

[5] G. Oliveri, P. Rocca, M. Salucci, and A. Massa, "Holographic smart EM skins for advanced beam power shaping in next generation wireless environments," *IEEE J. Multiscale Multiphys. Comput. Techn.*, vol. 6, pp. 171–182, 2021.

[6] G. Oliveri, F. Zardi, P. Rocca, M. Salucci, and A. Massa, "Building a smart EM environment–AI-enhanced aperiodic micro-scale design of passive EM skins," *IEEE Trans. Antennas Propag.*, early access, Feb. 21, 2022, doi: 10.1109/TAP.2022.3151354.

[7] W. Tang *et al.*, "Subject editor spotlight on programmable metasurfaces: The future of wireless," *IET Electron. Lett.*, vol. 55, no. 7, pp. 360–361, 2019.

[8] M. Di Renzo *et al.*, "Reconfigurable intelligent surfaces vs. relaying: Differences, similarities, and performance comparison," *IEEE Open J. Commun. Soc.*, vol. 1, pp. 798–807, 2020.

[9] J. C. Liang *et al.*, "An angle-insensitive 3-bit reconfigurable intelligent surface," *IEEE Trans. Antennas Propag.*, early access, Dec. 2021, doi: 10.1109/TAP.2021.3130108.

[10] P. Callaghan, P. Giannakou, S. G. King, M. Shkunov, and P. R. Young, "Linearly polarized reconfigurable reflectarray surface," *IEEE Trans. Antennas Propag.*, vol. 69, no. 10, pp. 6480–6488, Oct. 2021.

[11] F. Yang and Y. Rahmat-Samii, *Surface Electromagnetics with Applications in Antenna, Microwave, and Optical Engineering*. Cambridge, U.K.: Cambridge Univ. Press, 2019.

[12] P. Rocca *et al.*, "On the design of modular reflecting EM skins for enhanced urban wireless coverage," *IEEE Trans. Antennas Propag.*, early access, Feb. 2, 2022, doi: 10.1109/TAP.2022.3146870.

[13] A. Benoni, M. Salucci, G. Oliveri, P. Rocca, B. Li, and A. Massa, "Planning of EM skins for improved quality-of-service in urban areas," *IEEE Trans. Antennas Propag.*, early access, Jun, 2, 2022, doi: 10.1109/TAP.2022.3177284.

[14] J. A. Hodge, K. V. Mishra, and A. I. Zaghloul, "Intelligent time-varying metasurface transceiver for index modulation in 6G wireless networks," *IEEE Antennas Wireless Propag. Lett.*, vol. 19, pp. 1891–1895, 2020.

[15] A. Massa and M. Salucci, "On the design of complex EM devices and systems through the system-by-design paradigm: A framework for dealing with the computational complexity," *IEEE Trans. Antennas Propag.*, vol. 70, no. 2, pp. 1328–1343, Feb. 2022.

[16] S. Gong *et al.*, "Toward smart wireless communications via intelligent reflecting surfaces: A contemporary survey," *IEEE Commun. Surveys Tuts.*, vol. 22, no. 4, pp. 2283–2314, 4th Quart., 2020.

[17] A. Pitilakis*et al.*, "A multi-functional reconfigurable metasurface: Electromagnetic design accounting for fabrication aspects," *IEEE Trans. Antennas Propag.*, vol. 69, no. 3, pp. 1440–1454, Mar. 2021.

[18] L. Dai *et al.*, "Reconfigurable intelligent surface-based wireless communications: Antenna design, prototyping, and experimental results," *IEEE Access*, vol. 8, pp. 45913–45923, 2020.

[19] B. G. Kashyap, P. C. Theofanopoulos, Y. Cui, and G. C. Trichopoulos, "Mitigating quantization lobes in mmWave low-bit reconfigurable reflective surfaces," *IEEE Open J. Antennas Propag.*, vol. 1, pp. 604–614, 2020.

[20] C. Ross, G. Gradoni, Q. J. Lim, and Z. Peng, "Engineering reflective metasurfaces with ising Hamiltonian and quantum annealing," *IEEE Trans. Antennas Propag.*, vol. 70, no. 4, pp. 2841–2854, Apr. 2022, doi: 10.1109/TAP.2021.3137424.

[21] M. Salucci, A. Gelmini, G. Oliveri, N. Anselmi, and A. Massa, "Synthesis of shaped beam reflectarrays with constrained geometry by exploiting nonradiating surface currents," *IEEE Trans. Antennas Propag.*, vol. 66, no. 11, pp. 5805–5817, Nov. 2018.

[22] G. Oliveri, F. Viani, N. Anselmi, and A. Massa, "Synthesis of multilayer WAIM coatings for planar-phased arrays within the system-by-design framework," *IEEE Trans. Antennas Propag.*, vol. 63, no. 6, pp. 2482–2496, Jun. 2015.

[23] G. Oliveri, M. Salucci, N. Anselmi, and A. Massa, "Multiscale system-by-design synthesis of printed WAIMs for waveguide array enhancement," *IEEE J. Multiscale Multiphys. Comput. Tech.*, vol. 2, pp. 84–96, 2017.

[24] G. Oliveri, A. Gelmini, A. Polo, N. Anselmi, and A. Massa, "System-by-Design multiscale synthesis of task-oriented reflectarrays," *IEEE Trans. Antennas Propag.*, vol. 68, no. 4, pp. 2867–2882, Apr. 2020.

[25] G. Oliveri, A. Polo, M. Salucci, G. Gottardi, and A. Massa, "SbD-based synthesis of low-profile WAIM superstrates for printed patch arrays," *IEEE Trans. Antennas Propag.*, vol. 69, no. 7, pp. 3849–3862, Jul. 2021.

[26] M. A. Ricoy and J. L. Volakis, "Derivation of generalized transition/boundary conditions for planar multiple-layer structures," *Radio Sci.*, vol. 25, no. 4, pp. 391–405, Jul./Aug. 1990.

[27] K. Achouri, M. A. Salem, and C. Caloz, "General metasurface synthesis based on susceptibility tensors," *IEEE Trans. Antennas Propag.*, vol. 63, no. 7, pp. 2977–2991, Jul. 2015.

[28] J. A. Encinar and J. A. Zornoza, "Three-layer printed reflectarrays for contoured beam space applications," *IEEE Trans. Antennas Propag.*, vol. 52, no. 5, pp. 1138–1148, May 2004.

[29] D. R. Prado, M. Arrebola, M. R. Pino, and F. Las-Heras, "Complex reflection coefficient synthesis applied to dual-polarized reflectarrays with cross-polar requirements," *IEEE Trans. Antennas Propag.*, vol. 63, no. 9, pp. 3897–3907, Sep. 2015.

[30] P. Nayeri, F. Yang, and A. Z. Elsherbeni, "Design of single-feed reflectarray antennas with asymmetric multiple beams using the particle swarm optimization method," *IEEE Trans. Antennas Propag.*, vol. 61, no. 9, pp. 4598–4605, Sep. 2013.

[31] D. M. Pozar, S. D. Targonski, and R. Pokuls, "A shaped-beam microstrip patch reflectarray," *IEEE Trans. Antennas Propag.*, vol. 47, no. 7, pp. 1167–1173, Jul. 1999.

[32] A. Osipov and S. Tretyakov, *Modern Electromagnetic Scattering Theory With Applications*. Hoboken, NJ, USA: Wiley, 2017.

[33] M. Salucci, L. Tenuti, G. Oliveri, and A. Massa, "Efficient prediction of the EM response of reflectarray antenna elements by an advanced statistical learning method," *IEEE Trans. Antennas Propag.*, vol. 66, no. 8, pp. 3995–4007, Aug. 2018.

[34] P. Rocca, M. Benedetti, M. Donelli, D. Franceschini, and A. Massa, "Evolutionary optimization as applied to inverse problems," *Inverse Problems*, vol. 25, pp. 1–41, Dec. 2009.

[35] *ANSYS Electromagnetics Suite—HFSS*, ANSYS Inc., Canonsburg, PA, USA, 2021.

[36] H. Yang *et al.*, "A 1600-element dual-frequency electronically reconfigurable reflectarray at X/Ku-band," *IEEE Trans. Antennas Propag.*, vol. 65, no. 6, pp. 3024–3032, Jun. 2017.

[37] M. Ciydem and E. A. Miran, "Dual-polarization wideband sub-6 GHz suspended patch antenna for 5G base station," *IEEE Trans. Antennas Propag.*, vol. 19, no. 7, pp. 1142–1146, Jul. 2020.

[38] G. Oliveri, D. H. Werner, and A. Massa, "Reconfigurable electromagnetics through metamaterials—A review," *Proc. IEEE*, vol. 103, no. 7, pp. 1034–1056, Jul. 2015.

Giacomo Oliveri (Senior Member, IEEE) received the B.S. and M.S. degrees in telecommunications engineering and the Ph.D. degree in space sciences and engineering from the University of Genoa, Genoa, Italy, in 2003, 2005, and 2009, respectively.

He was a Visiting Researcher with the Laboratoire des signaux et systèmes (L2S), CentraleSupélec, Gif-sur-Yvette, France, in 2012, 2013, and 2015, an Invited Associate Professor with the University of Paris-Sud, Orsay, France, in 2014, and a Visiting Professor with Université Paris-Saclay, Bures-sur-Yvette, France, from 2016 to 2017. He is currently an Associate Professor with the Department of Civil, Environmental and Mechanical Engineering, University of Trento, Trento, Italy, where he is a Board Member of the ELEDIA Research Center. He is also an Adjunct Professor with CentraleSupélec, where he is a member of the L2S. He is the author/coauthor of over 400 peer-reviewed papers in international journals and conferences. His research work is mainly focused on electromagnetic direct and inverse problems, system-by-design and metamaterials, and antenna array synthesis.

Prof. Oliveri is the Chair of the IEEE AP/ED/MTT North Italy Chapter. He serves as an Associate Editor for the IEEE ANTENNAS AND WIRELESS PROPAGATION LETTERS, IEEE JOURNAL ON MULTISCALE AND MULTIPHYSICS COMPUTATIONAL TECHNIQUES, *EPJ Applied Metamaterials*, the *International Journal of Antennas and Propagation*, the *International Journal of Distributed Sensor Networks*, the *Microwave Processing* journal, and the *Sensors* journal.

Paolo Rocca (Senior Member, IEEE) received the M.S. degree *(summa cum laude)* in telecommunications engineering and the Ph.D. degree in information and communication technologies from the University of Trento, Trento, Italy, in 2005 and 2008, respectively.

He has been a Visiting Ph.D. Student with Pennsylvania State University, State College, PA, USA, and the Mediterranea University of Reggio Calabria, Reggio Calabria, Italy, and a Visiting Researcher with the Laboratoire des Signaux et Systèmes (L2S), CentraleSupélec, Gif-sur-Yvette, France, since 2012 and 2013, respectively. He has been an Invited Professor with the University of Paris-Sud, Orsay, France, since 2015, and the University of Rennes 1, Rennes, France, since 2017. He is currently an Associate Professor with the Department of Civil, Environmental, and Mechanical Engineering, University of Trento, and the Huashan Scholar Chair Professor with Xidian University, Xi'an, China, where he is a member of the ELEDIA Research Center. He is the author/coauthor of one book chapter, 150 journals, and more than 270 conference papers. His main interests are in the framework of artificial intelligence techniques as applied to electromagnetics, antenna array synthesis and analysis, and electromagnetic inverse scattering.

Prof. Rocca is also a member of the Big Data and AI Working Group for the Committee on Engineering for Innovative Technologies (CEIT) of the World Federation of Engineering Organizations (WFEO). He received the National Scientific Qualification for the position of Full Professor in Italy and France in April 2017 and January 2020, respectively. He has been awarded by the IEEE Geoscience and Remote Sensing Society and the Italy Section with the Best Ph.D Thesis Award of the IEEE-GRS Central Italy Chapter. He has served as an Associate Editor for the IEEE ANTENNAS AND WIRELESS PROPAGATION LETTERS from 2011 to 2016 and the *Microwave and Optical Technology Letters* (2019-2020). He has been serving as an Associate Editor for the *IEEE Antennas and Propagation Magazine* since 2020 and *Engineering* since 2020.

Marco Salucci (Senior Member, IEEE) received the M.S. degree in telecommunication engineering from the University of Trento, Trento, Italy, in 2011, and the Ph.D. degree from the International Doctoral School in Information and Communication Technology of Trento, University of Trento, in 2014.

He was a Post-Doctoral Researcher with CentraleSupélec, Paris, France, and the Commissariat à l'énergie atomique et aux énergies alternatives (CEA), Paris. He is currently a Researcher with the University of Trento, Trento, where he is a member of the ELEDIA Research Center. His research activities are mainly concerned with inverse scattering, biomedical and GPR microwave imaging techniques, antenna synthesis, and computational electromagnetics with a focus on system-by-design methodologies integrating optimization techniques and learning-by-examples methods for real-world applications.

Dr. Salucci was a member of the COST Action TU1208 "Civil Engineering Applications of Ground Penetrating Radar." He is a member of the IEEE Antennas and Propagation Society. He is an Associate Editor of Communications and Memberships of the IEEE TRANSACTIONS ON ANTENNAS AND PROPAGATION. He also serves as an Associate Editor for the IEEE TRANSACTIONS ON ANTENNAS AND PROPAGATION and a Reviewer for different international journals, including IEEE TRANSACTIONS ON ANTENNAS AND PROPAGATION, IEEE ANTENNAS AND WIRELESS PROPAGATION LETTERS, IEEE JOURNAL ON MULTISCALE AND MULTIPHYSICS COMPUTATIONAL TECHNIQUES, and *IET Microwaves, Antennas & Propagation*.

Danilo Erricolo (Fellow, IEEE) received the Laurea degree *(summa cum laude)* in electronics engineering from the Politecnico di Milano, Milan, Italy, in 1993, and the Ph.D. degree in electrical engineering and computer science from the University of Illinois at Chicago (UIC), Chicago, IL, USA, in 1998.

During the summer of 2009, he was an Air Force Faculty Fellow with the Air Force Research Laboratory, Wright-Patterson Air Force Base, Dayton, OH, USA. He is currently a Professor and the Director of Graduate Studies with the Department of Electrical and Computer Engineering, Director of the Andrew Electromagnetics Laboratory, and an Adjunct Professor of bioengineering with UIC. He has authored or coauthored more than 290 publications in refereed journals and international conferences. His research interests are primarily in the areas of antenna design, electromagnetic propagation and scattering, high-frequency techniques, wireless communications, electromagnetic compatibility, the computation of special functions, and magnetic resonance imaging.

Dr. Erricolo was an elected Full Member of Commissions B, C, and E of the U.S. National Committee (USNC) of the International Union of Radio Science (URSI), a committee of the U.S. National Academies. He was an elected member of the IEEE AP-S Administrative Committee from 2012 to 2014. He was a member at Large of USNC-URSI from 2012 to 2017. In 2017, he was nominated as a University of Illinois Scholar. He has served as the Chair, the Vice-Chair, and a Secretary of the USNC-URSI Commission E on Electromagnetic Environment and Interference from 2009 to 2011, 2006 to 2008, and 2004 to 2005, respectively. He was the Chair of the USNC-URSI Ernest K. Smith Student Paper Competition from 2009 to 2014 and the Vice-Chair of the Local Organizing Committee of the XXIX URSI General Assembly, held in Chicago, IL, USA, in August 2008. He was the Chair of the IEEE AP-S Distinguished Lecturer Program from 2015 to 2016 and the Chicago Joint Chapter of the IEEE AP-S and Microwave Theory and Techniques Society from 2011 to 2016. He was the General Chairperson of the 2012 IEEE International Symposium on Antennas and Propagation and the USNC-URSI National Radio Science Meeting, held in Chicago, in July 2012. He has served on more than 50 conference technical program committees, chaired over 70 conference sessions, and organized more than 30 special sessions at international scientific conferences. He has been the Editor-in-Chief of the IEEE TRANSACTIONS ON ANTENNAS AND PROPAGATION since August 2016.

Andrea Massa (Fellow, IEEE) received the Laurea (M.S.) degree in electronic engineering and the Ph.D. degree in electrical engineering and computer science (EECS) from the University of Genoa, Genoa, Italy, in 1992 and 1996, respectively.

He is currently a Full Professor of electromagnetic fields with the University of Trento, Trento, Italy, where he currently teaches electromagnetic fields, inverse scattering techniques, antennas and wireless communications, wireless services and devices, and optimization techniques. He is the Director of the network of federated laboratories "ELEDIA Research Center" located in Brunei, China, Czech Republic, France, Greece, Italy, Japan, Peru, and Tunisia with more than 150 researchers. Moreover, he is the holder of a Chang-Jiang Chair Professorship at the University of Electronic Science and Technology of China (UESTC), Chengdu, China, a Professor at CentraleSupélec, Gif-sur-Yvette, France, and a Visiting Professor at Tsinghua University, Beijing, China. He has been the holder of a Senior DIGITEO Chair at the Laboratoire des Signaux et Systèmes (L2S), CentraleSupélec, and Commissariat à l'énergie atomique et aux énergies alternatives - Laboratory for Integration of Systems and Technology (CEA LIST), Saclay, France, the UC3M-Santander Chair of Excellence at the Universidad Carlos III de Madrid, Getafe, Spain, an Adjunct Professor at Penn State University, State College, PA, USA, a Guest Professor at UESTC, and a Visiting Professor at the Missouri University of Science and Technology, Rolla, MO, USA, Nagasaki University, Nagasaki, Japan, the University of Paris-Sud, Orsay, France, Kumamoto University, Kumamoto, Japan, and the National University of Singapore, Singapore. He has organized more than 100 scientific sessions at international conferences and has participated in several technological projects in the national and international frameworks with both national agencies and companies (18 international projects: >5 M€; eight national projects: >5 M€; ten local projects: >2 M€; 63 industrial projects: >10 M€; and six university projects: >300 k€). He has published more than 900 scientific publications among which more than 350 on international journals ($>13\,500$ citations: H-index $=60$ [Scopus]; $>11\,000$ citations: H-index $=54$ [ISI-WoS]; and $>22\,000$ citations: H-index $=87$ [Google Scholar]) and more than 550 in international conferences where he presented more than 200 invited contributions (>40 invited keynote speaker). His research activities are mainly concerned with inverse problems, analysis/synthesis of antenna systems and large arrays, radar systems synthesis and signal processing, cross-layer optimization and planning of wireless/RF systems, semantic wireless technologies, system-by-design and material-by-design (metamaterials and reconfigurable-materials), and theory/applications of optimization techniques to engineering problems (telecommunications, medicine, and biology).

Dr. Massa is an IET Fellow and an Electromagnetic Academy Fellow. He is a member of the Editorial Board of the *Journal of Electromagnetic Waves and Applications*, a Permanent Member of the PIERS Technical Committee and the EuMW Technical Committee, and an ESoA member. He has been appointed to the Scientific Board of the Società Italiana di Elettromagnetismo (SIEm) and elected to the Scientific Board of the Interuniversity National Center for Telecommunications (CNIT). He has been appointed in 2011 by the National Agency for the Evaluation of the University System and National Research (ANVUR) as a member of the Recognized Expert Evaluation Group (Area 09, "Industrial and Information Engineering") for the evaluation of the research at the Italian University and Research Center for the period 2004–2010. Furthermore, he has been elected as the Italian Member of the Management Committee of the COST Action TU1208 "Civil Engineering Applications of Ground Penetrating Radar." He has been appointed as the IEEE AP-S Distinguished Lecturer from 2016 to 2018 and has served as an Associate Editor for the IEEE TRANSACTIONS ON ANTENNAS AND PROPAGATION (2011-2014). He serves as an Associate Editor for the *International Journal of Microwave and Wireless Technologies*.